DOI: 10.1002/ ((please add manuscript number))
Article type: Review

Inorganic Halide Perovskite Solar Cells: Progress and Challenges

Jingjing Tian[1], Qifan Xue[1,2], Qin Yao[1], Ning Li[3,4,5], Christoph J. Brabec[3,4], Hin-Lap Yip[1,2]**

J. Tian, Prof. Q. Xue, Q. Yao, Prof. H.-L. Yip
[1]State Key Laboratory of Luminescent Materials and Devices, Institute of Polymer Optoelectronic Materials and Devices, School of Materials Science and Engineering, South China University of Technology, 381 Wushan Road, Guangzhou, 510640, P. R. China.
E-mail: qfxue@scut.edu.cn. msangusyip@scut.edu.cn

Prof. Q. Xue, Prof. H.-L. Yip
[2]Innovation Center of Printed Photovoltaics, South China Institute of Collaborative Innovation, Dongguan 523808, P.R. China.

Dr. N. Li, Prof. C. Brabec
[3]Institute of Materials for Electronics and Energy Technology (i-MEET), Friedrich-Alexander-University Erlangen-Nuremberg, Martensstraße 7, 91058 Erlangen, Germany.
[4]Helmholtz Institut Erlangen Nürnberg (HI-ErN), Forschungszentrum Jülich, Immerwahrstrasse 2, D-91058 Erlangen, Germany.

Dr. N. Li
[5]National Engineering Research Center for Advanced Polymer Processing Technology, Zhengzhou University, 450002 Zhengzhou, China.

Keywords: lead-based and lead-free, inorganic perovskite solar cells, fundamental properties, progress, challenges

Abstract: All-inorganic perovskite semiconductors have recently drawn increasing attention owing to their outstanding thermal stability. Although all-inorganic perovskite solar cells (PSCs) have achieved significant progress in recent years, they still fall behind the prototype organic-inorganic counterparts owing to severer energy losses. Therefore, there is considerable interest in further improving the performance of all-inorganic PSCs by synergic optimization of perovskite films and device interfaces. This review article first provides an overview of recent progress in inorganic PSCs in terms of lead-based and lead-free composition. The physical properties of all-inorganic perovskite semiconductors

as well as the hole/electron transporting materials are discussed to unveil the important role of composition engineering and interface modification. Finally, a discussion of the prospects and challenges of all-inorganic PSCs in the near future is concluded.

1. Introduction

Energy scarcity and environmental pollution have become major barriers to realize the sustainable development in the future. So far, solar photovoltaic (PV) technology, which is the most effective way to solve these two problems at the same time, is the fastest growing research field in recent years. Among the various PV types, organic-inorganic hybrid perovskite solar cells (PSCs) have attracted enormous attention owing to their excellent optoelectronic properties. The general formula of hybrid perovskite materials is ABX_3, where A is a monovalent organic cation (such as $CH_3NH_3^+$ or MA^+; $CH_3(NH_2)_2^+$ or FA^+), B is a divalent metal cation (such as Pb^{2+}, Sn^{2+}, Ge^{2+}) and X is a monovalent halogen anion (I^-, Br^-, Cl^-).[1] After about 10 years of development, the certified power conversion efficiency (PCE) of organic-inorganic hybrid PSCs has reached 25.2%,[2] approaching that of the champion silicon solar cells (26.7%). Despite of the impressive performance, organic-inorganic hybrid PSCs still present significant challenges in terms of stability. Due to the hygroscopic and volatile nature of the organic cations, organic-inorganic hybrid perovskites suffer from chemical instability when exposed to oxygen, moisture, illumination and especially to high temperatures.[3-5] It is well known that inorganic materials are generally more stable than organic materials at high temperatures. Investigations have shown that the inorganic monovalent cation Cs^+ can satisfy the requirements of the ABX_3 structure, replacing MA^+ and FA^+ as the A-site ions to form high thermal stable $CsBX_3$ perovskites (>350°C). At the same time, $CsBX_3$ perovskite also is the best choice for preparation of

tandem solar cells because of the suitable wide bandgap.

Hence, research on all-inorganic halide perovskite $CsBX_3$ without any organic components has developed rapidly in the past few years, particularly in performance increasing from 10% to 19% within the last two years. The first all-inorganic halide PSCs based on $CsSnI_3$ using a Schottky junction structure (ITO/$CsSnI_3$/Au/Ti) were reported in 2012 to achieve a low PCE of 0.88%.[6] The performance was increased to 2.02% by using the standard device architecture (FTO/c-TiO_2/m-TiO_2/$CsSnI_3$/4,4',4"-tris(N,N-phenyl-3-methylamino) triphenylamine (m-MTDATA)/Au) in 2014.[7] Soon after, PSCs with more stable and efficient $CsPbX_3$ perovskites were developed with quickly improved PCE of over 10%.[8] At the time of writing, the PCE of optimized $CsPbI_3$ PSCs have reached 19.03% with a planar regular heterojunction structure FTO/c-TiO_2/$CsPbI_3$/Spiro-OMeTAD/Ag.[9] In addition to $CsBX_3$, many other types of all-inorganic halide perovskites have been theoretically predicted and synthesized.[10-12]

Owing to the fast development of all-inorganic PSCs, more and more research papers and strategies have been reported, yet there are still many knotty problems need to be solved. Both opportunities and challenges coexist for all-inorganic $CsBX_3$ PSCs. Therefore, a state-of-the-art and comprehensive review is urgently needed in this direction to summarize. In this review, we provide a systematic overview of recent progress in inorganic $CsBX_3$ PSCs. The related physical properties (such as ionic radius, carrier mobility, energy level structure) of the materials applied to $CsBX_3$ PSCs are firstly sorted out, including the $CsBX_3$ perovskites and hole/electron transporting materials. More importantly, a summarization of all-inorganic $CsBX_3$ PSCs (lead-based and lead-free) in detail is reviewed, containing all the important literatures and optimization strategies to date. Finally, the key problems of $CsBX_3$ PSCs are summarized and explained including large energy loss, ambient instability, crystal

defects, Pb-toxicity, weak theoretical foundation and so on. On how to solve these problems, we put forward some suggestions to the future development, for example, the synthesis of effective dopant-free transporting materials, the more efficient modification/passivation of perovskite defects, the new and simple preparation technology of devices, the improvement of theoretical foundation. The future development directions of $CsBX_3$ PSCs in photovoltaic applications are discussed as well.

2. Materials for $CsBX_3$ PSCs

The device architectures used for all-inorganic $CsBX_3$ PSCs include mesoscopic structure, planar heterojunction structure, and hole-transporting materials-free structure.[13] In recent years, the former two structures have been commonly used to achieve high PCEs. Regarding the planar heterojunctions, both n-i-p and p-i-n structures have been reported for PSCs, which are generally composed of an anode, a light-absorbing perovskite layer, an n-type electron transporting layer (ETL) and a p-type hole transporting layer (HTL), and a cathode, as illustrated in **Figure 1**. The working principle of PSCs is based on the photovoltaic effect of p-n junctions. Under solar irradiation, only photons with energy higher than the bandgap (Eg) of perovskite layer can be absorbed to generate electron-hole pairs, followed by carrier extraction of both electrons and holes due to the built-in electric fields or diffusion.[14] This intrinsic mechanism is actually suitable for both regular n-i-p and inverted p-i-n architectures.

2.1 $CsBX_3$ Perovskite Materials & Physical Properties

As direct bandgap materials, halide perovskites have a sharp absorption edge.[15] They can be processed from solution or by vacuum thermal evaporation, with broad spectrum absorption from the near infrared to the entire visible region, tunable and sharp emission (the full-width at half-maximum (FWHM) = 20~30 nm),[16] high photoluminescence quantum yield (PLQY) (>90%), long carrier

diffusion length (L_D >1 μm),[17] high carrier mobility, small exciton binding energy, tunable bandgap, balanced ambipolar transport, and high defect tolerance[18]. In addition, their component materials have abundant reserves.

For inorganic $CsBX_3$ perovskite materials, B site is still a divalent metal cation (such as Pb^{2+}, Sn^{2+}, Ge^{2+}, etc.) and X site is a monovalent halide (I^-, Br^- and Cl^-). The ideal crystal structure is cubic phase, as illustrated in **Figure 2a**. The B atom is located at the center of a regular octahedron of X atoms. The octahedron forms a three-dimensional network by sharing the vertices. Then the inorganic cation Cs^+ fills the octahedral space (**Figure 2b**), for instance, $CsPbI_3$, $CsPbBr_3$, $CsPbI_xBr_{3-x}$, $CsSnI_3$ and $CsSnBr_3$, are typical inorganic $CsBX_3$ compounds. In addition, some derivative structures of $CsBX_3$ perovskite materials have also been exploited, such as Cs_2BX_6 (including Cs_2SnI_6, Cs_2PbBr_6, Cs_2PbI_6), $Cs_3B_2X_9$ (including $Cs_3Sb_2I_9$, $Rb_3Sb_2I_9$, $Cs_3Bi_2I_9$) and $Cs_2B^{1+}B^{3+}X_6$ (including $Cs_2BiAgCl_6$, $Cs_2BiAgBr_6$).[10,19,20] **(Figure 2c)**

The formation and stability of the typical $CsBX_3$ perovskite structure are determined by two parameters: the Goldschmidt tolerance factor t, given by the **Equation (1)** and the octahedral factor μ (**Equation (2)**):

$$t = \frac{(r_{Cs}+r_X)}{\sqrt{2}(r_B+r_X)} \quad (1)$$

$$\mu = \frac{r_B}{r_X} \quad (2)$$

where r_{Cs}, r_B, and r_X are radii of corresponding ions. The range of t for perovskite phases is usually between 0.8 and 1.0, while the ideal range of μ for a geometrically stable perovskite phase is roughly $0.44 < \mu < 0.90$. On this condition, a cubic (α-, *Pm3m*) phase perovskite can be formed between $0.9 < t < 1.0$ or at high temperatures, while less symmetric tetragonal (β-, *P4/mbm*) or orthorhombic (γ-, *Pbnm*) phase perovskites are obtained for a lower t factor or at low temperatures **(Figure 3)**.[21-25] Here,

the radii of elements that have been used in $CsBX_3$ perovskites are summarized in **Table 1**. $CsPbBr_3$ undergoes the α- to β-phase and β- to γ-phase transitions at 130 °C and 88 °C, respectively, then could maintain stable γ-phase structure at room temperature.[26,27] Owing to the small $t \approx 0.81$ and $\mu \approx 0.55$, $CsPbI_3$ exhibits generally a yellow non-perovskite (δ-, *pnma*) phase at room temperature, and a stable black α-phase cannot be maintained due to lattice distortion. As a fact of matter, $CsPbI_3$ has three complicated black perovskite phases and one yellow non-perovskite phase: cubic (α-) (1.73 eV), tetragonal (β-) (1.68 eV), orthorhombic (γ-) (1.75 eV) perovskite phases and orthorhombic (δ-) (2.82 eV) non-perovskite phase.[28] When the temperature decreases gradually, $CsPbI_3$ undergoes the transition from black α- to β-phase at 281 °C and then to γ-phase at 184 °C. When black γ-phase $CsPbI_3$ is exposed to the humidity environment, it can transfer to non-perovskite δ-phase immediately.

The superior optoelectronic properties of cubic $CsBX_3$ perovskites, such as suitable optical bandgap, small exciton binding energy **(Figure 4a)**, long carrier diffusion length and large absorption coefficient ($>10^4$ cm^{-1}), make them the ideal light-harvesting materials for solar cell applications.

For perovskite materials, cubic phase is the most ideal crystal structure for the performance of PSCs due to perfect optoelectronic properties. The perovskite compositions decide their lattice constants, for example, 6.201 Å, 5.874 Å and 6.2057 Å are the cubic lattice constants of $CsPbI_3$, $CsPbBr_3$ and $CsSnI_3$ respectively. In addition to α-phase, γ-phase $CsPbI_3$ shows the unit cell dimensions a=8.8561±0.0004 Å, b=8.5766±0.0003 Å, c=12.4722±0.0006 Å.[29] Moreover, $CsSnI_3$ also exhibits other three polymorphs: one is a yellow one-dimensional (1D) orthorhombic structure (Y-$CsSnI_3$), one is a black three-dimensional (3D) tetragonal structure (B-β-$CsSnI_3$) and the other is a black 3D orthorhombic structure (B-γ-$CsSnI_3$). Y-$CsSnI_3$ (2.55 eV) (a=10.350 Å, b=4.7632 Å, c=17.684 Å) has nearly no photovoltaic response under solar light illumination, while B-γ-$CsSnI_3$ (1.3 eV) (a=8.6885 Å,

b=12.3775 Å, c=8.6384 Å) has excellent optical properties with high absorption in visible range. Meanwhile, B-γ-$CsSnI_3$ has a low exciton binding energy R* of 18 meV, and a quite high hole mobility of ~585 $cm^2\ V^{-1}\ s^{-1}$ and electron mobility of ~536 $cm^2\ V^{-1}\ s^{-1}$.[30-32] Experiments also found the R* of α-$CsPbI_3$ (15±1 meV) and α-$CsPbI_2Br$ (22±3 meV) is lower than γ-$CsPbBr_3$ (33±1 meV).[33] $CsPbX_3$ nanocrystals also attracted many research focus, with great optical characters including narrow emission widths of 12-42 nm, high PLQYs of 50-90% and short radiative lifetimes of 1-29 ns. Researchers further estimated the R* for $CsPbCl_3$ (75 meV), $CsPbBr_3$ (40 meV) and $CsPbI_3$ (20 meV).[34] It can be found that perovskite nanocrystals with small sizes have a larger exciton binding energy than 3D bulk perovskites. For carrier mobility, a fairly wide range from 10 to 4500 $cm^2\ V^{-1}s^{-1}$ for $CsPbX_3$ was reported, which may result from different measurement methods and material quality. Small values of ~25 $cm^2\ V^{-1}\ s^{-1}$, ~10 $cm^2\ V^{-1}\ s^{-1}$, ~38 $cm^2\ V^{-1}\ s^{-1}$ have been reported for $CsPbI_3$, $CsPbI_2Br$ and $CsPbBr_3$ polycrystalline film respectively.[35-38] A high electron mobility of 2290 $cm^2\ V^{-1}\ s^{-1}$ and the hole/electron mobilities of 2060/2240 $cm^2\ V^{-1}\ s^{-1}$ were calculated by the time-of-flight (TOF) technique and space-charge limited current (SCLC) method for $CsPbBr_3$ single crystal. By Hall effect measurement, a high electron mobility of 2270 $cm^2\ V^{-1}\ s^{-1}$ was obtained for $CsPbBr_3$ single crystals while nanocrystal films have a mobility of 77.9 $cm^2\ V^{-1}\ s^{-1}$.[39] Carrier diffusion length L_d of 1 μm, 80 nm and 16 nm were reported for solution-processed $CsPbI_3$, $CsPbBr_3$ and $CsSnI_3$ polycrystalline films, respectively.[32,36,40] $CsPbBr_3$ single crystal (10 μm for electrons and 12 μm for holes) and melt-synthesized $CsSnI_3$ film (1 μm) both showed a longer L_d than their polycrystalline films. For $CsPbI_3$, charge lifetime of >20 ns for spin-coated film and 10 μs for evaporated film were obtained.[35,36] Comparable with $CsPbI_3$ evaporated film, $CsPbBr_3$ single crystal also displayed a long lifetime of 2-7 μs, while $CsPbI_2Br$ (14 ns for spin-coated film) and $CsSnI_3$ (0.05-19.7 ns for spin-coated film and 6.6

ns for melt-synthesized film) both showed only several nanoseconds.[32,41] The dielectric constant (ε_{eff}) of $CsPbX_3$ is controlled by the lead halide cage at low temperature. From the study, the ε_{eff} of cubic α-$CsPbI_3$, α-$CsPbI_2Br$ and γ-$CsPbBr_3$ polycrystalline films were 10.0, 8.6 and 7.3 respectively.[33] **Table 2** summarizes the above relevant physical properties of representative $CsBX_3$ perovskites.

2.2 Hole/Electron Transporting Materials

The frequently-used hole transporting materials (HTM) in all-inorganic PSCs, such as 2,2',7,7'-tetrakis-(N,N-di-4-methoxyphenylamino)-9,9'-spirobifluorene (Spiro-OMeTAD), poly(3,4-ethylenedioxythiophene): poly(styrene-sulfonate) (PEDOT:PSS), poly[bis(4-phenyl)(2,4,6trimethylphenyl)amine] (PTAA) and NiO_x, could effectively transport holes and block electrons. The electron transporting materials (ETM) including TiO_2, SnO_2, ZnO and phenyl-C_{61}-butyric acid methyl ester (PCBM) could transfer electrons and block holes. However, the selection of HTL and ETL will significantly affect the performance of PSCs, which is mainly due to the energy-band alignment of the device structure and the operability of the processing solvents. The energy-band of HTM/ETM and their processing solvents are summarized in **Table 3** and **Figure 4b**.

As the most popular and efficient molecular HTM, Spiro-OMeTAD is employed frequently with two additives bis(trifluoromethylsulfonyl)amine lithium salt (LiTFSI) and 4-tert-butylpyridine (tBP) because of the low carrier mobility of intrinsic Spiro-OMeTAD. LiTFSI favors the oxidation and then the p-doping of Spiro-OMeTAD, and tBP molecules could prevent LiTFSI aggregation promoting a better interface contact between the HTM layer and perovskite layer. The hole mobility of doped Spiro-OMeTAD was estimated to be 3.32×10^{-3} cm^2 V^{-1} s^{-1}.[42] PEDOT:PSS is mainly applied into the p-i-n structure, with a high hole mobility of $>10^{-2}$ cm^2 V^{-1} s^{-1}. PTAA, which has conjugated chains and exhibits a rather high stability, is the main polymer HTM for both p-i-n and n-i-p type PSCs with high

efficiencies. Usually, PTAA also needs to be doped doped for improving its hole mobility (up to 10^{-2} cm^2 V^{-1} s^{-1}). NiO_x is an inorganic p-type semiconductor material with a hole mobility of 0.5 cm^2 V^{-1} s^{-1} and high chemical stability.[43]

TiO_2 exhibits typical n-type electrical conduction characteristics, and is the most widely used ETL in PSCs, simultaneously meeting two important conditions of high electron mobility (10^{-3} cm^2 V^{-1} s^{-1}) and stability. The compact TiO_2 layer can be produced by spray pyrolysis, thermal oxidation, atomic layer deposition and electrochemical deposition.[44] But during the fabrication process of TiO_2, a high-temperature annealing process (even up to 450°C) is essential and hinders its application on different substrates. Thus, inorganic SnO_2 and ZnO ETLs are developed that could be prepared at low temperature. The morphology and structure of ZnO used in PSCs mainly consist of dense planes and nanostructures. Nanostructure SnO_2 and ZnO have excellent electron mobility, about 100-200 cm^2 V^{-1} s^{-1} and 26 cm^2 V^{-1} s^{-1} respectively.[45,46] Apart from inorganic mental oxides, organic small molecule PCBM with an electron mobility of 2×10^{-3} cm^2 V^{-1} s^{-1} is commonly applied to the p-i-n device structure.[47]

3. High-Performance All-Inorganic $CsBX_3$ PSCs

3.1 Lead-Based $CsBX_3$ PSCs

Lead-based $CsBX_3$ PSCs have experienced rapid development in the past several years, stimulated by the wide variety of perovskite compositions. The first report on $CsPbX_3$ materials actually dates back to 1893, followed by a report on crystal structure and photo-conductivity in 1958.[27] In this section, we highlight recent progress in high-efficiency $CsPbX_3$ PSCs mainly based on $CsPbI_3$, $CsPbBr_3$, and $CsPbI_xBr_{3-x}$. Corresponding photovoltaic parameters reported in recent years are summarized in **Table 4**, which shows the rapid increase in PCEs.

3.1.1 $CsPbI_3$ PSCs

$CsPbI_3$ typically exhibits a yellow non-perovskite phase at room temperature and a black cubic perovskite phase with a band gap of 1.73 eV that is stable at high temperatures but very unstable at room temperature.[48] The first $CsPbI_3$ PSC was reported by Choi and his colleagues in 2014.[49] They attempted to remove MA^+ from $Cs_xMA_{1-x}PbI_3$ solar cells, resulting in a low PCE of only 0.09%.

Soon after, Eperon et al. applied the black phase α-$CsPbI_3$ in PSCs for the first time.[50] By processing in an inert atmosphere, and developing a low temperature phase transition route (adding a small amount of hydroiodic acid HI to the $CsPbI_3$ precursor solution), they obtained $CsPbI_3$ films that were stable in the black phase at room temperature. The addition of HI induced the formation of smaller grains with enhanced lattice strain, and therefore increased phase transition at low temperatures, as shown in **Figure 5a-5b**. They fabricated solar cells in a variety of architectures, and achieved a PCE of 2.9% for a planar heterojunction PSC. As described above, smaller grain size can cause lattice strain to partially stabilize the α-$CsPbI_3$ phase.

Swarnkar et al. used small nanocrystals (NCs) to further stabilize the α-$CsPbI_3$ black phase and achieved a PCE of 10.77% with a open-circuit voltage (V_{OC}) of 1.23 V **(Figure 5c-5d)**.[8] They provided an improved approach for synthesizing and purifying the $CsPbI_3$ QDs that retain the cubic phase for months in ambient air and even at cryogenic temperatures. The perovskite films fabricated using the $CsPbI_3$ QDs could achieve efficient dot-to-dot electronic transport while retaining the phase stability of the individual QDs. Subsequently, other additives have been developed to reduce the grain size, such as ascorbic acid (AA),[51] poly-vinylpyrrolidone (PVP)[52] and sulfobetaine zwitterions (including NDSB201, NDSB211 and SB3-10),[53] as displayed in **Figure 5e-5f**.

In addition to controlling the grain size, element doping has also been used to stabilize the α-$CsPbI_3$.

Hu et al. engineered the composition of $CsPbI_3$ by incorporating Bi^{3+} to stabilize the α-$CsPbI_3$ at room temperature, achieving a significantly high stability and a high PCE of 13.21% with 4 mol.% Bi^{3+}.[54] The control of the Bi ratio in the precursor solution is critical for complete transformation from the δ-phase to the α-phase and the final device performance. Many metal ions have been incorporated into the B-site of $CsPbI_3$, including Sn^{2+},[55,56] Ca^{2+},[57] Mn^{2+},[58] Eu^{3+},[59] and Sb^{3+},[60] to improve the undesired Goldschmidt tolerance factor (t). The A-site doping by Na-element was also reported.[61] **(Figure 6)**

Besides the metal ion-doping, engineering of the A-site composition with organic ions has also been adopted in recent years, resulting in stable two-dimensional (2D) perovskite structures **(Figure 7a-7b)**. Zhang et al. reported that a small amount of 2D $EDAPbI_4$ perovskite containing the ethylenediamine (EDA) cation stabilized the α-$CsPbI_3$ by suppressing the formation of the undesirable non-perovskite δ-phase.[62] Jiang et al. added a judicious amount of phenylethylammonium iodide (PEAI) to induce inorganic quasi-2D perovskites, $PEA_2Cs_{n-1}Pb_nI_{3n+1}$, which greatly suppressed undesirable phase transition and reduced the film's trap-state density, resulting in an impressive PCE of 12.4% with greatly improved longevity.[63]

Recently, Wang et al. obtained a stable α-$CsPbI_3$ film with high quality by controlling the growth of perovskite thin films in a dry environmental condition **(Figure 7c-7d)**. The PCE of PSCs was significantly increased to 15.7%, and remained unchanged under continuous illumination for more than 500 hours.[64] It was found by Wang et al. that a post-treatment with phenyltrimethylammonium bromide (PTABr) could result in a gradient Br doping (or alloying) and surface passivation. The PTABr treatment on $CsPbI_3$ induced a blue-shift in UV-vis absorbance of less than 5 nm but significantly improved the stability of the perovskite phase. The highly stable PTABr-treated $CsPbI_3$ PSCs exhibited

a remarkably high efficiency of up to 17.06% and a stable power output of 16.3%.[65] Apart from PTABr, PEAI was also applied as a defect-passivation agent to improve the phase stability and moisture resistance.[66] **(**see **Figure 7e-7f)**

Lately, theoretical calculations predicted that the black tetragonal (β-) and orthorhombic (γ-) phase $CsPbI_3$ would have a more stable perovskite structure than the cubic α-phase, as shown in **Figure 8**. Wang et al. prepared a distorted black phase (lower-symmetry orthorhombic) γ-$CsPbI_3$ film by exploiting the synergistic effect of HI and PEAI additives.[67] They found that HI induced the formation of hydrogen lead iodide ($HPbI_{3+x}$), an intermediate to the distorted black phase with an appropriate band gap of 1.69 eV; while PEAI provided nucleation for optimized crystallization. More importantly, the PEAI stabilized the distorted black phase by hindering phase transition via its steric effects. The optimized PSCs achieved a high PCE of 15.07% with a remarkable device stability. In a very recent study, Wang et al. obtained highly crystalline β-$CsPbI_3$ films with an extended spectral response and an enhanced phase stability.[68] To further mitigate the effects of cracks and pinholes in the perovskite layer, they introduced choline iodide (CHI) by surface treatment to boost the PCE of $CsPbI_3$ PSCs to 18.4% under 45 ± 5°C ambient conditions.[68] The PCE was further improved to a champion value of 19.03% by employing phenyltrimethylammonium chloride (PTACl) to passivate the $CsPbI_3$ films.[9] They revealed that most of the previously reported the X-ray diffraction (XRD) patterns that have been incorrectly indexed to the α-$CsPbI_3$ phase actually correspond to the γ-$CsPbI_3$, in accordance with the large bandgap of ~1.73 eV of the latter system, as illustrated in **Figure 9**. This discovery is of great significance to guide the future work on all-inorganic PSCs.

3.1.2 $CsPbBr_3$ PSCs

$CsPbBr_3$ is another important inorganic perovskite with the same crystal structure as $CsPbI_3$. The

only difference between them is that the X-site anion (I^-) is replaced with Br^-, which has a smaller ionic radius. Consequently, the yellow orthorhombic-phase $CsPbBr_3$ is stable at room temperature owing to the proper Goldschmidt tolerance factor t. Normally, $CsPbBr_3$ can transform to the yellow tetragonal phase and yellowish-orange cubic phase at 88℃ and 130℃, respectively.[26,27] This compound is recognized as the most stable lead halide perovskite material under the ambient conditions. The band gap of $CsPbBr_3$ is increased to 2.3 eV (that of $CsPbI_3$ is 1.73 eV), making it an excellent candidate for tandem or semitransparent solar cells. However, the photocurrent density of $CsPbBr_3$ PSCs is relatively low owing to the limited absorption in the range of 300-540 nm. In 2015, Kulbak et al. firstly fabricated the mesoporous $CsPbBr_3$ PSCs in a structure of FTO/c-TiO_2/m-TiO_2/$CsPbBr_3$/ HTL/Au. The best PCE of 5.95% was obtained by using PTAA HTL.[69] Soon after, they prepared a stable $CsPbBr_3$ PSC by two-step sequential deposition technique, in which the $PbBr_2$ layer was first deposited by spin coating, then the substrates were dipped in the CsBr solution, followed by annealing for 10 minutes at 250 °C under a N_2 stream.[70] In their aging studies at 15-20% RH, the PCE of $CsPbBr_3$ PSCs with a device structure of FTO/d-TiO_2/mp-TiO_2/$CsPbBr_3$/PTAA/Au exhibited no significant decrease after two weeks, but the PCE of $MAPbBr_3$ decreased to ~15% of its initial value. The remarkable stability of $CsPbBr_3$ can be attributed to the elimination of the organic component MABr, which is much more volatile than CsBr and would result in the decomposition of perovskite under operational conditions.

Although inorganic perovskites exhibited a superior stability to their hybrid counterparts, the utilization of organic HTMs still restricted their long-term stability. For example, the organic small molecule Spiro-OMeTAD promoted decomposition of the perovskite layer, owing to the unstable dopants used. In addition, the thermal stability of most organic materials is poor, which limits their practical use. Thermal-stable metal oxide materials, such as NiO_x, MoO_x and VO_x, have been used to

replace organic HTMs, but their application is hindered by low electrical conductivity. Considering the outstanding optoelectronic properties of inorganic perovskite, it is feasible to fabricate the HTL-free inorganic PSCs because the fact that they could also achieve photon absorption and hole transport without the organic HTLs. Chang et al. developed $CsPbBr_3$-based HTM-free PSCs based on a typical structure of FTO/TiO_2/$CsPbBr_3$/Carbon, as displayed in **Figure 10a**.[71] After a careful optimization, the PCE of their devices reached 5.0% with a V_{OC} of 1.29 V. Note that they used a carbon electrode rather than the usual Ag or Au, for the following reasons: first, the halide ions in the perovskite materials have been shown to react easily with metal electrodes, even Ag and Au; second, the water-resistance of carbon materials is better than that of Au; and finally, the price of carbon is much lower than that of Au, which is beneficial to the commercialization of PSCs. Carbon-based $CsPbBr_3$ PSCs is much more stable than $CH_3NH_3PbI_3$. After storage at 80 °C for 250 h, the former lost only 11.7% of its initial PCE, while the latter exhibited a loss in PCE by 59%. Similar work was also reported by Liang et al.[72] The PCEs of 6.7% and 5.0% were achieved for devices (FTO/c-TiO_2/m-TiO_2/$CsPbBr_3$/carbon) with small (0.12 cm^2) and large active area (1.0 cm^2), respectively. Even without encapsulation, the PSCs presented no performance degradation in humid air (90-95% RH, 25 °C) for over 3 months and can endure extreme temperatures (100 and -22 °C). Recently, Duan et al. demonstrated the simplified architecture of FTO/$CsPbBr_3$/carbon for $CsPbBr_3$ PSCs, achieving an efficiency of 4.1% along with a promising stability through interfacial modification by graphene quantum dots (GQDs) and $CsPbBrI_2$ quantum dots (PQDs).[73] These studies showed that in terms of long-term stability, especially thermal stability, carbon-based HTM-free $CsPbBr_3$ PSCs are more promising, opening the door for next-generation PSCs with long-term stability under practical conditions.

$CsPbBr_3$ films were commonly prepared by a two-step sequential deposition technique. However, due to large concentration differences between CsBr (the maximized concentration of CsBr in methanol is about 0.07 M) and $PbBr_2$ solutions (the concentration of $PbBr_2$ in DMF can reach 1 M), the quality of $CsPbBr_3$ films is significantly limited by current solution-processing techniques, always forming mixed phases (like Cs_4PbBr_6 and $CsPbBr_3$) in the corresponding perovskite films. Thus, Duan et al. developed a new multistep solution-processing method to achieve $CsPbBr_3$ perovskite films with high quality and purity.[74] A $PbBr_2$ (1 M) DMF solution was spin-coated onto the ETL to form a solid $PbBr_2$ layer and then CsBr (0.07 M) in ethanol was further spin-coated on $PbBr_2$ layer for 4 times, as illustrated in **Figure 10b**. With increasing the CsBr spin-coating times, the crystal phase of inorganic halides converted from $CsPb_2Br_5$ ($n \leq 3$) to $CsPbBr_3$ ($n = 4$) and subsequently to Cs_4PbBr_6 ($n \geq 5$). A ~5 nm thick GQDs layer was inserted between ETL and $CsPbBr_3$ to modify the interface, leading to a champion PCE of 9.72% with excellent humidity and thermal stability.

It is essential for all-inorganic $CsPbBr_3$ PSCs to further improve their PCEs by, for instance, enlarging their optical absorption. Partial substitution of Br ions with I ions to form $CsPbBr_xI_{3-x}$ ($0 < x < 3$) is a good way to solve this problem, which will be discussed in detail in the next section. Another crucial factor limiting their performance is the serious charge recombination within perovskite film. A-site lattice doping of $CsPbBr_3$ with alkali metal cations (Li^+, Na^+, K^+, and Rb^+) has been proven to be an effective way to suppress non-radiative loss and radiative recombination **(Figure 10c-16f)**.[75] Recently, the lattice doping of lanthanide ions into $CsPbBr_3$ films was also investigated by Duan et al.[76] They used a multistep solution-processed method to dope Ln^{3+} (=La^{3+}, Ce^{3+}, Nd^{3+}, Sm^{3+}, Eu^{3+}, Gd^{3+}, Tb^{3+}, Ho^{3+}, Er^{3+}, Yb^{3+} and Lu^{3+}) into $CsPbBr_3$ films and characterized the perovskite films **(Figure 10g-10i)**. Ln^{3+} ions were successfully incorporated into host $CsPbBr_3$ lattice, and the grain

size of Sm^{3+} doped film increased to 1 μm compared to that of pristine $CsPbBr_3$ layer (~500 nm). The larger grain size of Ln^{3+}-doped $CsPbBr_3$ might arise from the strong interaction between Ln^{3+} and Br^-, which led to the Ln^{3+} capping layer surrounding on the surface and grain boundaries during the crystal growth, changing the surface energy to increase perovskite crystallization. In addition, time-resolved photoluminescence (TRPL) revealed that Ln^{3+} doping could significantly prolong the lifetime of charge carriers. An impressively high PCE of 10.14% with an ultrahigh V_{OC} of 1.594 V was obtained for PSCs in a device architecture of FTO/c-TiO_2/m-TiO_2/$CsPb_{0.97}Sm_{0.03}Br_3$/carbon. More important, these devices showed excellent long-term stability even under 80% humidity or at 80°C.

While the quality of perovskite films is easily affected by the solution-processing conditions, it is very attractive to use perovskite colloidal NCs, with which the quality of perovskite films is largely independent of processing conditions. The size and the quality of NCs can be well controlled during synthesis, however, it is not easy to convert the NCs into solid films while preserving their properties. The bulky ligands and the residual chemicals would form an insulating layer around the NCs, preventing the formation of compact films and obstructing carrier migration. Akkerman et al. used short and low-boiling-point ligands, including propionic acid (PrAc) and butylamine (BuAm), and environmentally friendly solvents, including isopropanol (IPrOH) and hexane (HEX), for the synthesis of $CsPbBr_3$ NCs, as illustrated in **Figure 11a**.[77] The photoluminescence quantum yield (PLQYs) of these $CsPbBr_3$ NCs (15-20 nm) films were higher than those prepared using long alkyl chains, showing that the non-radiative recombination process could be successfully suppressed. Requiring no lengthy post-synthesis treatments, the $CsPbBr_3$ NCs were directly used to fabricate films of high optoelectronic quality. After optimizing the film thickness through nine sequential depositions, the PSCs exhibited a PCE of 5.4% with a V_{OC} as high as 1.5 V, indicating the high quality of $CsPbBr_3$ nanocrystal films.

Zhou et al. reported a novel carbon quantum dot (CQD)-embedded $CsPbBr_3$ inverse opal (IO) structure, developed by using a facile template-assisted spin-coating method using the structure of FTO/TiO_2/CQD-$CsPbBr_3$ IO/Spiro-OMeTAD/Ag.[78] The preparation process is shown in **Figure 11b**. Due to the slow-photon effect and light scattering by the 3D mesoporous structure of photonic crystals, the light absorption of the perovskite film was greatly improved **(**see **Figure 11c-11d)**. It is worth noting that the CQDs embedded in the film acted as a visible light sensitizer that broadened the light absorption of the perovskite film, with a red-shifted absorption onset at about 550 nm. The PSCs based on CQD-embedded $CsPbBr_3$ IO film exhibited a remarkable PCE of 8.29%, double that of devices based on planer $CsPbBr_3$ film.

Inorganic QDs, such as $CuInS_2$/ZnS QDs,[79,80] GQDs,[73,80] PQDs,[73] $CsMBr_3$ (M=Sn, Bi, Cu) QDs,[81] and $CsSnBr_{3-x}I_x$ QDs[82] have also been chosen to modify the ETL/$CsPbBr_3$ and $CsPbBr_3$/carbon interface to improve the charge carrier extraction and suppress recombination, as shown in **Figure 11e-11g**. Duan et al. introduced p-type inorganic Cu(Cr,M)O_2 (M = Ba^{2+}, Ca^{2+}, or Ni^{2+}) nanocrystals at $CsPbBr_3$/carbon interface, effectively extracting holes from perovskite by increasing interstitial oxygen.[83] The $CsPbBr_3$ PSCs with a device structure of FTO/c-TiO_2/m-TiO_2/$CsPbBr_3$/Cu(Cr,Ba)O_2/carbon achieved an efficiency of 10.18%, which was further improved to 10.79% by doping 3% Sm^{3+} ions into perovskite. The unencapsulated Cu(Cr,Ba)O_2-based PSCs presented a remarkable stability in air under either 80% humidity over 60 days or 80°C conditions over 40 days or light illumination for 7 days.[83] In addition, 15 nm thick CsBr and $PbBr_2$ were evaporated on the TiO_2 layer by Qian et al. to achieve excellent optoelectronic properties for TiO_2/CsBr/$CsPbBr_3$ and TiO_2/$PbBr_2$/$CsPbBr_3$ hetero-structure interfaces.[84]

Li et al. introduced excess $PbBr_2$ into the $CsPbBr_3$ layer by precisely controlling the thickness of

CsBr and $PbBr_2$ in the vapor system. After post-annealing, the derivative phase $CsPbBr_3$-$CsPb_2Br_5$ coexisted in the perovskite film. $CsPb_2Br_5$ at the $CsPbBr_3$ grain boundaries could effectively passivate the defects and lower the energy barrier, achieving a high humidity-stable PSC with a PCE of 8.34% and a high V_{OC} of 1.296 V **(Figure 11h)**.[85] And Wang et al. also successfully obtained smooth and dense $CsPbBr_3$ films via NH_4SCN additive engineering with great crystallinity and low trap state density.[86]

With respect to the application in tandem solar cells, Chen et al. combined a $CsPbBr_3$ top cell with an organic bottom cell **(**see **Figure 11i-11j)**.[87] The $CsPbBr_3$ film was prepared by a dual-source vacuum co-evaporation method, greatly reducing the defects during film preparation. The $CsPbBr_3$-based PSCs exhibited a PCE of 7.78% and a high V_{OC} of 1.44 V. Moreover, the $CsPbBr_3$ top cell can absorb UV light, acting as a UV filter, which contributed to the protection of the bottom organic solar cell. The optimized tandem cell exhibited a PCE of 14.03% with great photo-stability. After 120 h of UV-light illumination, the device maintained more than 99.4% of its initial PCE.

3.1.3 $CsPbI_xBr_{3-x}$ PSCs

The black α-$CsPbI_3$ phase is extremely unstable at room temperature, and the band gap of stable $CsPbBr_3$ is relatively too large (2.3 eV). Researchers therefore began to prepare mixed halide perovskite $CsPbI_xBr_{3-x}$ by partially replacing iodine (2.2 Å) with the bromine (1.96 Å) to stabilize the desired phase at low temperatures. Sutton et al.[88] and Beal et al.[89] studied $CsPbI_xBr_{3-x}$ materials with x in the range of 0-1, and found that the band gap decreased with increasing x value. The partial substitution of I with Br at room temperature contributed to stabilizing the perovskite phase, and $CsPbI_2Br$ PSCs were found to be highly stable at high temperatures.

Doping of metal elements into the A-site or B-site of perovskite composition was used to modify

the optoelectronic properties of $CsPbI_xBr_{3-x}$ **(Figure 12)**. By partially replacing the A-site Cs^+ with K^+, Nam et al. reported the enhanced electron lifetime in $Cs_{1-x}K_xPbI_2Br$ film without affecting the light absorption range, leading to an optimized PCE of ~10% and improved environmental stability.[90] With respect to the B-site doping, Lau et al. incorporated a small amount of Sr^{2+} into $CsPbI_2Br$ to form $CsPb_{1-x}Sr_xI_2Br$ perovskite.[91] Enriched Sr element was found on the surface of the perovskite film, possibly forming Sr oxide, which was beneficial to passivate defects. Finally, the charge recombination in the device was sufficiently suppressed and the electron lifetime was increased, which increased the PCE from 7.7% to 11.2%. By partially replacing the Pb^{2+} with Sn^{2+}, Li et al. reported a high efficiency of 11.53% for $CsPbIBr_2$ PSCs with excellent stability.[92] In addition, many other metal ions have been employed to dope the B-site of $CsPbI_xBr_{3-x}$ perovskites, such as Sn^{2+},[93] Mn^{2+},[94,95] Eu^{2+},[96] In^{3+},[97,98] Cu^{2+},[99] Ge^{2+},[100] Ba^{2+},[101] and Zn^{2+} [102,103]. Among them, Subhani et al. demonstrated that Ba(II) dopant can also be used to substitute the B-site Pb to achieve high photovoltaic performance, even though the Ba atom is too large to obey the Goldschmidt rule,[101] as shown in **Figure 12i**. Xiang et al. reported a similar work on the addition of Ba to the $CsPbI_2Br$ perovskite precursor. However, they found that the substitution of Pb^{2+} with Ba^{2+} in the perovskite lattice was negligible. The reduced bandgap was due to the large difference between the ionic radii of Ba^{2+} (1.35 Å) and Pb^{2+} (1.20 Å). In fact, the Ba^{2+} segregated into Br-based non-perovskite phases, leading to an increased I/Br ratio in the perovskite layer **(Figure 12j-12k)**.[104] These results contributed to the rapid progress of the research about all-inorganic PSCs.

Interface engineering is a commonly used strategy to optimize the energy level alignment within PSCs and passivate the surface defects of perovskite films. Yan et al. introduced the use of solution-processed ZnO nanoparticles between the $CsPbI_2Br$ light-absorbing layer and a SnO_2 ETL

(SnO_2/ZnO/$CsPbI_2Br$). The well aligned energy levels at the interfaces enhanced the electron extraction capability and reduced the charge carrier recombination in the light-absorbing layer, leading to a high PCE of 14.6% for optimized $CsPbI_2Br$ PSCs in a device architecture of glass/ITO/SnO_2/ZnO/$CsPbI_2Br$/Spiro-OMeTAD/MoO_3/Ag **(Figure 13a)**.[105] Recently, Li et al. used a solvothermal method to synthesize the core-shell ZnO@SnO_2 nanoparticles, which showed superior electron mobility to the pristine SnO_2 nanoparticles and better matched energy levels with $CsPbI_2Br$ perovskite.[106] The optimized $CsPbI_2Br$ PSCs based on the ZnO@SnO_2 ETL achieved a high PCE of 14.35% along with a current density (J_{SC}) of 16.45 mA cm^{-2}, a V_{OC} of 1.11 V and a fill factor (FF) of 79%. Zeng et al. replaced the Spiro-OMeTAD layer with a thin poly(3-hexylthiophene) (P3HT) layer, which with low energy disorder can passivate the defect states on the surface of $CsPbI_2Br$ film, resulting in a high V_{OC} of 1.32 V and a low E_{loss} of 0.5 eV **(Figure 13b-13e)**.[107] In addition, Liu et al. studied the energy level alignment at the ETL/$CsPbI_2Br$ interface in a p-i-n device architecture of FTO/NiOx/$CsPbI_2Br$/ZnO@C60/Ag,[108] where ZnO@C60 bilayer were utilized as the ETL with efficient carrier extraction and low leakage loss, as illustrated in **Figure 13f**. The PCE of optimized $CsPbI_2Br$ PSCs reached 13.3% with an improved long-time thermal stability.

Apart from the optimization of charge transport layer, numerous strategies have been developed to modify and/or passivate the surface. For instance, the introduction of a thin LiF layer (~3 nm)[109], bismuth telluride (Bi_2Te_3) nanoplates[110] and an ultra-thin dye molecule YD_2-o-C8 layer[111] to modify the ETL/$CsPbI_xBr_{3-x}$ or $CsPbI_xBr_{3-x}$/Spiro-OMeTAD interface, the utilization of lewis base small molecule 6TIC-4F to passivate surface defects $CsPbI_xBr_{3-x}$ perovskite film,[112] the evaporation of CsBr to passivate the $CsPbI_2Br$/HTL interface,[113] the use of anti-solvents, such as chlorobenzene (CB),[114,115] isopropanol (IPA),[114] dichloromethane (DCM),[114] toluene (TOL),[114] ethyl acetate

(EA),[114,115] and diethyl ether (DEE),[114] and the modification of organic iodized salts and perovskite QDs, such as MAI, FAI, and GAI,[114,116] $CsPbI_2Br$ QDs,[116] and $CsPbI_3$ QDs[117] to achieve high quality $CsPbIBr_2$ and $CsPbI_2Br$ films. Lately, an amino-functionalized polymer (PN4N) as the cathode interlayer and a dopant-free HTL poly[5,5′-bis(2-butyloctyl)-(2,2′-bithiophene)-4,4′-dicarboxylate-alt5,5′-2,2′-bithiophene] (PDCBT) as the anode interlayer were applied to modify and passivate the SnO_2/$CsPbI_2Br$ and $CsPbI_2Br$/HTL interfaces, respectively.[118] PN4N and PDCBT could have strong interaction with the $CsPbI_2Br$ perovskite, which effectively passivated the electronic surface defects and suppressed the photo-induced halide segregation of $CsPbI_2Br$ films, as shown in **Figure 13g**. The optimized $CsPbI_2Br$ PSCs exhibited a PCE of over 16% with great photo-stability, which is one of the highest efficiencies reported for $CsPbI_2Br$ PSCs at present.

Wang et al. obtained a PCE of 16.14% for $CsPb(I_{0.85}Br_{0.15})_3$ PSCs based on a solvent-controlled precursor thin film growth method.[64] Chen et al. used a gradient thermal annealing (GTA) method to control the growth of α-$CsPbI_2Br$ crystals, and a green anti-solvent (ATS) IPA to further optimize the morphology of $CsPbI_2Br$ films **(Figure 14a)**.[119] They found that the growth of $CsPbI_2Br$ crystals could be precisely controlled to form a high-quality perovskite film with an average grain size of 1 μm and a low defect density, leading to a maximum PCE of 16.07% (stabilized PCE of 15.75%). Most importantly, the $CsPbI_2Br$ PSCs showed excellent resistance to moisture and oxygen, and maintained 90% of their initial PCE after 120 h under 100 mW/cm^2 UV irradiation. In addition to the control of crystallization processes, excess CsI/CsBr/PbI_2[120,121] in the perovskite film was also reported to be an effective approach to fabricate inorganic perovskites with low trap states and high crystallinity.

Recently, Guo et al. fabricated a PBDTTT-E-T:IEICO layer as a near-infrared light absorber on the ultraviolet-visible light $CsPbI_2Br$ absorber to broaden the absorption spectrum of all-inorganic solar

cells and improve their PCE,[122] as illustrate in **Figure 14b**. Owing to the additional absorption, the integrated solar cells exhibited an obviously enhanced J_{SC} from 14.78 to 15.98 mA/cm^2, resulting in an improved PCE of 14.03% with excellent air stability and thermal stability. Combining an all-inorganic perovskite with an organic active layer could be a promising method to further improve the PCE and stability of all-inorganic PSCs.

Furthermore, developing reliable and scalable process for perovskite film production is an essencial approach to achieve future commercialization.[123,124] Lau et al. have used a spray-assisted deposition process to fabricate $CsPbIBr_2$ films for PSCs with a stabilized PCE of 6.3% and negligible hysteresis.[125] Apart from spray coating, blade coating was also deployed to fabricate $CsPbI_2Br$ PSCs under ambient conditions by Fan et al., achieving the PCE of 14.69% (0.03 cm^2) and 12.52% (1.00 cm^2).[126] **(Figure 14c-14d)**

3.2 Lead-Free $CsBX_3$ PSCs

Today, the efficiency of PSCs has reached 25.2%. In 2017, Grancini et al. assembled a 2D/3D hybrid PSC that maintained its performance for more than one year.[127] The high PCE and stability of PSCs suggested that their commercialization is possible. Lead (Pb) is an essential component of high-efficiency PSCs, but it is also well known to be extremely harmful to humans and the environment. So far, the toxicity issue of lead-based PSCs is still an unresolved problem. There is an urgent need to reduce or eliminate Pb from the whole photovoltaic devices. As a consequence, it is of great importance to develop all-inorganic lead-free PSCs. In principle, other less-toxic as well as environmentally friendly metals, such as Sn, Ge, Bi, Ag, Ti and Na, could be the suitable substitutions of Pb element. Despite plenty of lead-free all-inorganic perovskites with various structures have been reported, the performance of PSCs is quite low. Herein, several types of all-inorganic lead-free PSCs are mainly

discussed, including $CsSnI_3$, $CsSnBr_3$, $CsSnI_xBr_{3-x}$ and $CsGeX_3$.

3.2.1 $CsSnI_3$ PSCs

Tin (Sn) is regarded as one of the most suitable replacements for Pb, as Sn^{2+} has similar ionic radius and chemical properties to Pb^{2+}. $CsSnI_3$ has two structural forms at room temperature: Y-$CsSnI_3$ (yellow phase with one-dimensional double-stranded structure) and B-γ-$CsSnI_3$ (black rhombohedral phase). B-γ-$CsSnI_3$ exhibits a band gap of 1.3 eV, high absorption coefficient and low exciton binding energy, which make it a great candidate for application in PSCs. After the first report by Chen et al. on $CsSnI_3$ PSCs using a Schottky junction structure,[6] Kumar et al. demonstrated $CsSnI_3$-based PSCs in a device architecture of FTO/compact TiO_2/mesoporous TiO_2/$CsSnI_3$/HTM/Au in 2014.[7] The perovskite layer was deposited by a one-step solution method at ~70°C. Using DMF and 2-methoxyethanol as solvents led to the formation of island-like perovskite crystals, while a high coverage of $CsSnI_3$ film was achieved by using DMSO. The easy oxidation of Sn^{2+} to Sn^{4+} and the formation of Sn vacancies are fatal problems for tin-based PSCs. Therefore, 20% SnF_2 was added to suppress the generation of vacancies and the oxidation of Sn^{2+}, resulting in a PCE of 2.02% with a J_{SC} of 22.70 mA/cm^2, a V_{OC} of 0.24 V and a FF of 37%.

In general, $CsSnI_3$-based PSCs can be successfully fabricated via a solution process, but exhibit low photovoltaic performance due to high trap-assisted recombination caused by poor morphology and the existence of massive Sn vacancies. Wang et al. utilized a solvent mixture containing acetonitrile, DMF and methoxyactonitrile to dissolve the $CsSnI_3$ solid materials.[128] A uniform, coarse-grained B-γ-$CsSnI_3$ perovskite film was obtained via post-annealing **(**see **Figure 15a)**. The optimized annealing temperature was 150°C, and higher temperature could introduce lots of Sn vacancies, serving as charge recombination centers in $CsSnI_3$ layer. The PCE of $CsSnI_3$ device based on Al_2O_3 was only 0.32%,

which was attributed to the poor crystallinity of the perovskite film and the ill-contacted interface between perovskite and insulating mesoporous Al_2O_3. By replacing Al_2O_3 with high-quality pinhole-free nickel oxide (NiO_x) layer, the optimized PCE of B-γ-$CsSnI_3$ PSCs reached up to 3.31% with a V_{OC} of 0.52 V, a J_{SC} of 10.21 mA/cm^2, and a FF of 0.625.

To obtain an ideal $CsSnI_3$ perovskite layer, many efforts have been focused on solving the easy oxidation of Sn^{2+}. Marshall et al. investigated the influence of excess SnI_2/$SnBr_2$/$SnCl_2$/SnF_2 on the morphology of $CsSnI_3$ film and the performance of PSCs.[129] $SnCl_2$ was found to have the greatest positive influence on the efficiency and stability of PSCs, because a $SnCl_2$ thin layer could form at the surface of the perovskite film and grain boundary. The HTL-free $CsSnI_3$ PSC with 10mol% $SnCl_2$ (structure: ITO/$CsSnI_3$+$SnCl_2$/$PC_{61}BM$/bathocuproine (BCP)/Al) exhibited a PCE of 3.56% with satisfied device stability. When $CsSnI_3$ perovskite film was exposed to air, the $SnCl_2$ layer formed stable $SnCl_2{\cdot}2H_2O$ and SnO_2, which prevented further infiltration of water and oxygen **(**see **Figure 15b)**. However, Heo et al. found that $SnBr_2$ was the best additive for their $CsSnI_3$ PSCs. The 10mol% $SnBr_2$-$CsSnI_3$ device showed a PCE of 4.30% with a high stability under RT and RH=40% due to the similar surface passivation effect to $SnCl_2$.[130]

Song et al. demonstrated an approach based on reducing vapor atmosphere of hydrazine (N_2H_4) to prevent short-circuit behavior and achieve well-functioning $CsSnI_3$ PSCs with a maximum PCE of 4.81%.[131]

Very recently, Chen et al. prepared highly stable and efficient all-inorganic lead-free PSCs with a native-oxide passivation method,[132] in which a $CsSn_{0.5}Ge_{0.5}I_3$ perovskite composition was synthesized using the melt-crystallization method and the $CsSn_{0.5}Ge_{0.5}I_3$ perovskite thin film was deposited by a single-source evaporation method, as displayed in **Figure 15c-15f**. They found that a

uniform layer of native-oxide GeO_2 doped with a small portion of Sn (<5nm) formed on the surface of the $CsSn_{0.5}Ge_{0.5}I_3$ perovskite thin films when exposed to air, passivating the perovskite and enhancing the moisture stability. Besides, the passivation layer also served as a wide-bandgap interfacial layer between the perovskite film and the HTL. Under its synergistic effect, lead-free $CsSn_{0.5}Ge_{0.5}I_3$ PSCs delivered a high efficiency of 7.11%, the highest value reported so far for all-inorganic lead-free PSCs, and a promising stability in N_2 atmosphere under one-sun illumination.

3.2.2 $CsSnBr_3$ PSCs

The substitution of X elements in $CsSnX_3$ also changes the band gap of perovskite materials. By replacing the I elements in $CsSnI_3$ with Br, the band gap of perovskite increases from 1.30 to 1.75 eV.[133] Gupta et al. used a one-step solution method to prepare $CsSnBr_3$ PSCs in a device architecture of FTO/d-TiO_2/m-TiO_2/$CsSnBr_3$+SnF_2/Spiro-OMeTAD/Au.[134] The optimized $CsSnBr_3$-based PSCs with 20mol% SnF_2 reached a PCE of 2.17% and a V_{OC} of 0.42 V. Song et al. developed an effective process to reduce the vapor atmosphere (N_2H_4) during the preparation of $CsSnBr_3$ (+20mol% SnF_2) PSCs, as shown in **Figure 15g-15h**.[135] A possible reaction path during the preparation of $CsSnBr_3$ was $2SnI_6^{2-}+N_2H_4 \rightarrow SnI_4^{2-}+N_2+4HI$, reverting the perovskite back to ideal semiconducting behavior. The Sn^{4+}/Sn^{2+} ratio was largely decreased leading to greatly suppressed carrier recombination, and thus a PCE of 3.04%. Besides, similar approach was also reported by adding SnF_2 as an additive.[136,137]

3.2.3 $CsSnI_xBr_{3-x}$ PSCs

The PCE of $CsSnI_3$-based PSCs is much lower than that of their lead-based counterparts, which can be attributed to the low band gap (1.30 eV) of $CsSnI_3$, which is the origin of high photocurrent densities, but also the bottleneck restricting its V_{OC}. To solve this issue, Sabba et al. modulated the V_{OC} by

chemically doping $CsSnI_3$ with Br, leading to the formation of $CsSnI_xBr_{3-x}$ ($0 \leq x \leq 3$) perovskite.[136] The band gap of $CsSnI_3$ increased from 1.27 to 1.37, 1.65 and 1.75 eV for $CsSnI_2Br$, $CsSnIBr_2$ and $CsSnBr_3$, respectively. Note that the V_{OC} increased from 0.201 V for $CsSnI_3$ to 0.410 V for $CsSnBr_3$, due to the increased bandgap and the reduced charge recombination. The addition of 20mol% SnF_2 hindered the generation of Sn vacancies, thus further reducing the background carrier density. It was found that PSCs based on $CsSnI_{2.9}Br_{0.1}$ exhibited the best performance among $CsSnI_xBr_{3-x}$ PSCs with an efficiency of 1.76% and a J_{SC} of 24.16 mA/cm^2.

Except the SnX_2 additive, Li et al. reported a novel additive hypophosphorous acid (HPA) for the preparation of the phase-stable $CsSnIBr_2$ perovskite film with a significantly reduced concentration of Sn vacancies.[138] As a complexant, HPA could not only accelerate the nucleation process, but also inhibit the formation of Sn^{4+} during $CsSnIBr_2$ perovskite film deposition. Consequently, the addition of HPA remarkably suppressed the vacancy-induced charge recombination. The $CsSnIBr_2$ PSCs achieved an optimized PCE of 3.20%, with the greatly enhanced V_{OC}, FF as well as a superior thermal stability.

3.2.4 $CsGeX_3$ PSCs

$CsGeX_3$ is another promising perovskite material for photovoltaic applications. Theoretical calculations have shown that $CsGeX_3$ has high absorption properties, and similar electron/hole transport properties and absorption spectra to the lead-based counterparts.[139] As is well known, the bandgap of perovskite materials largely depends on the halide ion, so that the bandgaps of $CsGeI_3$, $CsGeBr_3$ and $CsGeCl_3$ are 1.53, 2.32 and 3.67 eV, respectively. Among these compounds, $CsGeI_3$ is a potential light absorber in PSCs. However, similar to Sn^{2+}, the Ge^{2+} in perovskite is also easily oxidized to Ge^{4+}, which makes it difficult to obtain ambient-stable $CsGeI_3$ perovskite film. Furthermore, it is

difficult to test devices in air. Krishnamoorthy et al. first reported $CsGeI_3$-based PSCs in a device architecture of FTO/TiO_2/$CsGeI_3$/Spiro-OMeTAD/Au.[140] Smooth $CsGeI_3$ perovskite films can be obtained by using DMF as the solvent in the precursor solution **(**see **Figure 15i-15k)**. In this study, $CsGeI_3$-based PSCs exhibited a J_{SC} of 5.7 mA/cm^2, a V_{OC} of 0.074 V, a FF of 27% and a PCE of 0.11%. The relatively low V_{OC} and FF might be attributable to the presence of Ge^{4+}. Owing to the great challenge, the development of $CsGeX_3$ PSCs is relatively slow at present.

3.2.5 Other derivatives PSCs

In "Lead-Free $CsBX_3$ PSCs" this section, we mainly focus on the above four perovskite types: $CsSnI_3$, $CsSnBr_3$, $CsSnI_xBr_{3-x}$ and $CsGeX_3$. In order to better understand the progress of lead-free perovskites, other perovskite derivatives are also discussed in this part although most of their PSCs exhibit low efficiencies: $Cs_2SnI_{6-x}Br_x$ (2.025%),[141] Cs_2TiBr_6 (3.3%),[142] Cs_2NaBiI_6 (0.42%),[143] $Cs_2AgBiBr_6$ (2.51%),[144] $Cs_3Bi_2I_9$ (3.2%),[145] $Cs_3Sb_2I_9$ (1.49%)[146]. In the following, we briefly introduce the progress of the most common members $Cs_2AgBiBr_6$ and $Cs_2SnI_{6-x}Br_x$ PSCs.

The halide double perovskite structure $Cs_2B'B''X_6$ could be formed by replacing two toxic Pb^{2+} in the crystal lattice with a pair of nontoxic heterovalent metal cations (including one monovalent B^+ and one trivalent B^{3+}) and is a promising alternative to fabricate lead-free, high-efficiency and stable PSCs. $Cs_2AgBiBr_6$ perovskite exhibits an indirect bandgap of about 1.9-2.2 eV and could be simply prepared via a solution method. Greul et al. introduced the $Cs_2AgBiBr_6$ film into PSCs for the first time by a fast spin-coating method: both the precursor solution and the substrate were preheated to 75 °C and the hot precursor solution was spin-coated onto the substrate, following by thermal annealing at a high temperature of 285 °C to avoid the other phases such as $Cs_3Bi_2Br_9$ and form the desired pure double perovskite phase. The fabricated $Cs_2AgBiBr_6$ PSCs exhibited a promising PCE close to 2.5%.[147] Apart

from the traditional solution method, Wang et al. demonstrated a sequential vapor deposition method to realize high-quality double perovskite films. They firstly deposited AgBr onto the substrate, subsequently deposited $BiBr_3$ and CsBr on top of the AgBr film, followed by a two-step thermal annealing to form the double $Cs_2AgBiBr_6$ perovskite film through diffusion reaction. The optimized PSC showed a PCE of 1.37% and great device stability maintaining 90% initial efficiency after 240 h storage in air.[148] Recently, Igbari et al. found that solution-processing method is better than vacuum-evaporation because solution process could achieve a precise composition stoichiometry to form high-quality film which leads to the optimized PCE of 2.51%, while vacuum-evaporation method is 1.41%.[144] Apparently, the performance of Cs_2AgBiX_6 solar cells is still poor at the present time, mainly owing to their indirect and large bandgap. Thus it is significant to develop other double perovskite materials with direct bandgaps, such as $Cs_2AgInBr_6$ (1.33 eV direct bandgap).[31,149]

$Cs_2SnI_{6-x}Br_x$ perovskites derive from $CsSnI_{3-x}Br_x$ perovskite structure by removing half of Sn^{2+}, in which Sn is the tetravalent cation (Sn^{4+}). Cs_2SnI_6 with a direct bandgap of 1.48 eV and high absorption coefficient can be formed by spontaneous oxidation of $CsSnI_3$ film in ambient air. It has been proven by Jiang et al. that the Cs_2SnI_6 film could be stable at a high temperature (270°C) or in high relative humidity because the Sn in this compound is in the stable 4+ oxidation state. But they found that there are a large number of defects and unbalanced carrier transport in Cs_2SnI_6 film leading to a low PCE of 0.47%.[150] Lee et al. prepared efficient $Cs_2SnI_{6-x}Br_x$ thin films through optimizing the I/Br ratio and annealing process. They adopted a sandwich-type device structure (FTO/TiO_2/2wt% Sn-TiO_2/$Cs_2SnI_4Br_2$/Solid state Cs_2SnI_6 based HTM/electro-sprayed large-effective-surface-area polyaromatic hydrocarbon (LPAH)/FTO), exhibiting a promising PCE of 2.025% and a higher stability (50 days in air) than Cs_2SnI_6 PSCs.[141]

4. Challenges and Opportunities

Without the thermal instability issue of volatile and hygroscopic organic cations, the latest developments of all-inorganic halide PSCs over the recent years have shown much progress as a promising alternative to organic-inorganic hybrid PSCs. We summarize the annual number of published periodical articles on all-inorganic PSCs, as shown in **Figure 16a**. It is obvious that there are more and more researchers put their focus on all-inorganic perovskite. Although the PCE of all-inorganic $CsPbI_3$ PSCs has increased to over 19%, their performance is still non-ideal and approaches only 70% of the Shockley-Queisser (S-Q) efficiency limit. By contrast, the latest certified PCE (25.2%) of the organic-inorganic hybrid PSCs has reached over 80% of the S-Q limit, as illustrated in **Figure 16b**. Moreover, the PCE of the lead-free PSCs is very low (PCE of 7.11%). Meanwhile, most of the all-inorganic perovskite materials like $CsPbI_3$ and $CsSnI_3$ still suffer from chemical degradation under ambient atmosphere, mostly resulting from polymorphic transformation or oxidation. As a consequence, the most urgent things in the future are to achieve much higher PCEs and solve the structural stability. While the existing strategies could mitigate these two issues to some extent, there is still plenty of room for further improvement in this area. The following research directions could be of great significance for further enhancing the performance of all-inorganic materials and devices:

(1) **Figure 16c** shows the relationship between the PCE and the corresponding V_{OC} of the high efficiency $CsPbX_3$ PSCs. And **Figure 16d** gives the relationship between these V_{OC} and the corresponding Shockley-Queisser efficiency limit of $CsPbX_3$ PSCs. The energy loss of $CsPbX_3$ PSCs is relatively serious (> 0.6 V), which is the main reason limiting the further improvement of the device efficiency, caused by mismatched energy levels and high defect density and low carrier lifetime. Firstly, for mismatched energy levels in the PSC, energy barriers will be generated to prevent effective carrier

extraction and transfer. The development of HTM and ETM with more suitable energy levels and design of the novel architectures (such as SnO_2/ZnO-$CsPbI_2Br$) for all-inorganic perovskite materials can greatly promote charge transfer. Secondly, the quality of perovskite crystallites plays a crucial role in the device performance. In general, there will be a large number of crystal defects in the interior and surface of perovskite films, including shallow level defects and deep level defects. These defects will act as the charge recombination centers, accelerating the hole and electron recombination, reducing carrier lifetime, and increasing energy losses. Among them, deep level defects such as anti-site occupations have more adverse effects.[151] We can explore new progresses that can precisely control the compositions/microstructures of perovskite thin films at the nanoscale, and continue exploring new molecular materials as additives or interface materials to effectively passivate grain boundaries or surface defects. At the same time, more perfect crystal structure with fewer defects are also important to improve the structural stability of all-inorganic perovskites.

(2) Apart from optimizing crystallization to improve chemical stability, stable charge transport materials and stable electrode materials are also important. We can design and develop new dopant-free transport materials to replace the commonly used doped Spiro-OMeTAD to improve stability, such as P3HT and PDCBT. In addition, electrode materials (such as carbon electrode) can not only allow better charge extraction, but also provide device encapsulation function.

(3) At the same time, it is significant to strengthen basic theoretical research into all-inorganic halide perovskites. Systematic theoretical simulations and modelling are required to explain the experimental results. With the help of high-throughput artificial intelligence processes, design and development of next generation all-inorganic materials in the future can be foreseen. Moreover, we can learn the degradation mechanism of all-inorganic perovskites by means of advanced in-situ characterization

techniques based on synchrotron and transmission electron microscope (TEM), understanding the role of defects, crystal morphology, grain boundaries and orientation in the degradation of all-inorganic perovskites. We can also simulate the optimized device structures, materials and thickness of each structure layers, providing more authoritative reference for our experiments. For instance, the energy bands, photo-generation rate, J-V characteristics, and spectral response of the devices with different architectures can be calculated by Silvaco technology computer-aided design (TCAD) simulation code; the first-principle calculations implemented in the Vienna Ab initio simulation package (VASP) codes can be employed to investigate the interfacial properties based on electronic and atomic structures.[152]

(4) Similar to organic-inorganic hybrid perovskites, lead-based all-inorganic halide perovskites are still the main direction, although lead is toxic to humans and environment. However, the research on non-toxic, lead-free all-inorganic halide perovskites has slowly progressed. Further systematic studies are needed to focus on lead-free Sn-based all-inorganic PSCs. All strategies discussed above can be utilized to optimize the lead-free Sn-based all-inorganic PSCs.

In addition to the improvement of its own device performance, all-inorganic halide perovskite is also very suitable for silicon-perovskite tandem solar cells, which show great promise in industrial applications in the future. The band gap of crystalline silicon is approximately 1.1 eV, thus in order to obtain a silicon-perovskite tandem solar cell with a high PCE, the all-inorganic halide perovskite requires a band gap of ~1.75 eV to absorb as much light as possible. The band gaps of $CsPbBr_3$ and $CsPbI_3$ are 2.3 eV and 1.73 eV, respectively, indicating that the band gap of $CsPbI_{3-x}Br_x$ can be adjusted between 1.73 and 2.3 eV by adjusting the halide composition. The all-inorganic perovskites are also suitable for other tandem solar cells, for instance, all-perovskite tandem solar cells and organic photovoltaic (OPV)-perovskite tandem solar cells. We believe hybrid tandem solar cells based on all-

inorganic PSCs will have great potentials and will trigger more research interests in the next few years.

It can be seen from **Table 4** and **Table 5** that the all-inorganice PSCs are mainly based on the n-i-p device architecture. However, the p-i-n device architecture is very attractive owing to their easy fabrication, cost-effectiveness, and suppressed hysteresis characteristics.[153] However, the PCE of inverted PSCs is low and their V_{OC} loss is large, mainly due to the lack of suitable charge transporting materials. Although a huge number of ETMs (such as C_{60}, $PC_{61}BM$) and HTMs (such as CuSCN, CuO_2, GO) materials even the bi-layer structures of ETMs (such as $PC_{61}BM$/BCP, $PC_{61}BM$/poly[(9,9-bis(3'-(N,N-dimethylamion)propyl)-2,7-fluorene)-alt-2,7-(9,9-dioctyl)-fluorene] (PFN), $PC_{61}BM$/ZnO) or HTMs (such as PEDOT:PSS/poly[N,N'-bis(4-butylphenyl)-N,N'-bis(phenyl)benzidine] (Poly-TPD) MoO_3/PEDOT:PSS) have been developed for organic-inorganic hybrid PSCs,[153-156] they are all not perfectly appropriate for application in all-inorganic PSCs, because of the high annealing temperature of all-inorganic perovskites and the unmatched energy levels, etc. Consequently, novel interface materials are still required for developing all-inorganic PSCs with high efficiency and high stability.

In summary, all-inorganic halide perovskites have developed rapidly over the past three years and have shown a great potential in photovoltaic applications. It has great development prospects and requires more efforts to achieve the best solar cell performance and device stability. For all-inorganic PSCs, challenges and opportunities coexist in the future.

Acknowledgements
The work was financially supported by the Ministry of Science and Technology (No. 2017YF0206600), the Basic and Applied Basic Research Major Program of Guangdong Province (No. 2019B030302007), the Natural Science Foundation of China (Nos. 21761132001, 91733302 and 51803060), the Science and Technology Program of Guangdong Province, China (No. 2018A030313045) and the Science and Technology Program of Guangzhou, China (No. 2017A050503002). N.L. gratefully acknowledges the financial support from the DFG research grant: BR 4031/13-1. C.J.B. gratefully acknowledges the financial support through the "Aufbruch Bayern" initiative of the state of Bavaria (EnCN and SFF),

the Bavarian Initiative “Solar Technologies go Hybrid” (SolTech) and the SFB 953 (DFG, project no. 182849149).

Received: ((will be filled in by the editorial staff))
Revised: ((will be filled in by the editorial staff))
Published online: ((will be filled in by the editorial staff))

References

[1] J.-H. Im, I.-H. Jang, N. Pellet, M. Grätzel, N.-G. Park, *Nature Nanotech.* **2014**, *9*, 927.

[2] Research Cell Efficiency Records. NREL (*http://www.nrel.gov/ncpv/*). Accessed on September, ***2019***.

[3] K. O. Brinkmann, J. Zhao, N. Pourdavoud, T. Becker, T. Hu, S. Olthof, K. Meerholz, L. Hoffmann, T. Gahlmann, R. Heiderhoff, M. F. Oszajca, N. A. Luechinger, D. Rogalla, Y. Chen, B. Cheng, T. Riedl, *Nat. Commun.* **2017**, *8*, 13938.

[4] S. Chen, X. Wen, S. Huang, F. Huang, Y.-B. Cheng, M. Green, A. Ho-Baillie, *Solar RRL* **2017**, *1*, 1600001.

[5] Y. Guo, X. Yin, J. Liu, S. Wen, Y. Wu, W. Que, *Solar RRL* **2019**, *3*, 1900135.

[6] Z. Chen, J. J. Wang, Y. Ren, C. Yu, K. Shum, *Appl. Phys. Lett.* **2012**, *101*, 093901.

[7] M. H. Kumar, S. Dharani, W. L. Leong, P. P. Boix, R. R. Prabhakar, T. Baikie, C. Shi, H. Ding, R. Ramesh, M. Asta, M. Graetzel, S. G. Mhaisalkar, N. Mathews, *Adv. Mater.* **2014**, *26*, 7122.

[8] A. Swarnkar, A. R. Marshall, E. M. Sanehira, B. D. Chernomordik, D. T. Moore, J. A. Christians, T. Chakrabarti, J. M. Luther, *Science* **2016**, *354*, 92.

[9] Y. Zhao, Y. Wang, X. Liu, T. Zhang, X. Wang, M. Kan, J. Shi, *Angew. Chem. Int. Ed.* **2019**, *58*, 16691.

[10] F. Giustino, H. J. Snaith, *ACS Energy Lett.* **2016**, *1*, 1233.

[11] J. Wang, H. Chen, S. H. Wei, W. J. Yin, *Adv. Mater.* **2019**, *31*, e1806593.

[12] W. Ning, F. Gao, *Adv. Mater.* **2019**, *31*, e1900326.

[13] Y. Wu, P. Wang, S. Wang, Z. Wang, B. Cai, X. Zheng, Y. Chen, N. Yuan, J. Ding, W.-H. Zhang, *ChemSusChem* **2018**, *11*, 837.

[14] W. Tress, *Organic-Inorganic Halide Perovskite Photovoltaics, Springer* **2016**, pp.53.

[15] S. De Wolf, J. Holovsky, S.-J. Moon, P. Löper, B. Niesen, M. Ledinsky, F.-J. Haug, J.-H. Yum, C. Ballif, *J. Phys. Chem. Lett.* **2014**, *5*, 1035.

[16] J. Song, J. Li, X. Li, L. Xu, Y. Dong, H. Zeng, *Adv. Mater.* **2015**, *27*, 7162.

[17] S. D. Stranks, G. E. Eperon, G. Grancini, C. Menelaou, M. J. P. Alcocer, T. Leijtens, L. M. Herz, A. Petrozza, H. J. Snaith, *Science* **2013**, *342*, 341.

[18] Q. A. Akkerman, G. Rainò, M. V. Kovalenko, L. Manna, *Nature Mater.* **2018**, *17*, 394.

[19] S. F. Hoefler, G. Trimmel, T. Rath, *Monatshefte für Chemie - Chemical Monthly* **2017**, *148*, 795.

[20] H. Chen, S. Xiang, W. Li, H. Liu, L. Zhu, S. Yang, *Solar RRL* **2018**, *2*, 1700188.

[21] Z. Li, M. Yang, J.-S. Park, S.-H. Wei, J. J. Berry, K. Zhu, *Chem. Mater.* **2015**, *28*, 284.

[22] J. A. Steele, H. Jin, I. Dovgaliuk, R. F. Berger, T. Braeckevelt, H. Yuan, C. Martin, E. Solano, K. Lejaeghere, S. M. J. Rogge, C. Notebaert, W. Vandezande, K. P. F. Janssen, B. Goderis, E. Debroye, Y. Wang, Y. Dong, D. Ma, M. Saidaminov, H. Tan, Z. Lu, V. Dyadkin, D. Chernyshov, V. V. Speybroeck, E. H. Sargent, J. Hofkens, M. B. J. Roeffaers, *Science* **2019**, *365*, 679.

[23] F. Igbari, Z. K. Wang, L. S. Liao, *Adv. Energy Mater.* **2019**, *9*, 1803150.

[24] L. N. Quan, B. P. Rand, R. H. Friend, S. G. Mhaisalkar, T. W. Lee, E. H. Sargent, *Chem. Rev.* **2019**, *119*, 7444.

[25] J. Liang, J. Liu, Z. Jin, *Solar RRL* **2017**, *1*, 1700086.

[26] C. C. Stoumpos, C. D. Malliakas, J. A. Peters, Z. Liu, M. Sebastian, J. Im, T. C. Chasapis, A. C. Wibowo, D. Y. Chung, A. J. Freeman, B. W. Wessels, M. G. Kanatzidis, *Cryst. Growth Des.* **2013**, *13*, 2722.

[27] C. K. MØLler, *Nature* **1958**, *182*, 1436.

[28] Q. Ye, Y. Zhao, S. Mu, P. Gao, X. Zhang, J. You, *Sci. China Chem.* **2019**, *62*, 810.

[29] R. J. Sutton, M. R. Filip, A. A. Haghighirad, N. Sakai, B. Wenger, F. Giustino, H. J. Snaith, *ACS Energy Lette.* **2018**, *3*, 1787.

[30] I. Chung, J. H. Song, J. Im, J. Androulakis, C. D. Malliakas, H. Li, A. J. Freeman, J. T. Kenney, M. G. Kanatzidis, *J. Am. Chem. Soc.* **2012**, *134*, 8579.

[31] X. Li, J. Wu, S. Wang, Y. Qi, *Chem. Lett.* **2019**, *48*, 989.

[32] M. Konstantakou, T. Stergiopoulos, *J. Mater. Chem. A* **2017**, *5*, 11518.

[33] Z. Yang, A. Surrente, K. Galkowski, A. Miyata, O. Portugall, R. J. Sutton, A. A. Haghighirad, H. J. Snaith, D. K. Maude, P. Plochocka, R. J. Nicholas, *ACS Energy Lett.* **2017**, *2*, 1621.

[34] L. Protesescu, S. Yakunin, M. I. Bodnarchuk, F. Krieg, R. Caputo, C. H. Hendon, R. X. Yang, A. Walsh, M. V. Kovalenko, *Nano Lett.* **2015**, *15*, 3692.

[35] E. M. Hutter, R. J. Sutton, S. Chandrashekar, M. Abdi-Jalebi, S. D. Stranks, H. J. Snaith, T. J. Savenije, *ACS Energy Lett.* **2017**, *2*, 1901.

[36] S. Dastidar, S. Li, S. Y. Smolin, J. B. Baxter, A. T. Fafarman, *ACS Energy Lett.* **2017**, *2*, 2239.

[37] C. L. Kennedy, A. H. Hill, E. S. Massaro, E. M. Grumstrup, *ACS Energy Lett.* **2017**, *2*, 1501.

[38] H. Zhu, M. T. Trinh, J. Wang, Y. Fu, P. P. Joshi, K. Miyata, S. Jin, X. Y. Zhu, *Adv. Mater.* **2017**, *29*, 1603072.

[39] J. Deng, J. Li, Z. Yang, M. Wang, *J. Mater. Chem. C* **2019**, *7*, 12415.

[40] M. Kulbak, I. Levine, E. Barak-Kulbak, S. Gupta, A. Zohar, I. Balberg, G. Hodes, D. Cahen, *Adv. Energy Mater.* **2018**, *8*, 1800398.

[41] J. Zhang, G. Hodes, Z. Jin, S. F. Liu, *Angew. Chem. Int. Ed.* **2019**, *58*, 15596.

[42] Q. Xiao, J. Tian, Q. Xue, J. Wang, B. Xiong, M. Han, Z. Li, Z. Zhu, H. L. Yip, Z. Li, *Angew. Chem. Int. Ed.* **2019**, *58*, 17724.

[43] S. Xiao, F. Xu, Y. Bai, J. Xiao, T. Zhang, C. Hu, X. Meng, H. Tan, H. P. Ho, S. Yang, *Solar RRL* **2018**, *3*, 1800278.

[44] J. Wang, Y. Liu, X. Chen, C. Chen, P. Chen, Z. Wang, Y. Duan, *Chemphyschem* **2019**, *20*, 2580.

[45] X. Zhang, J. Liang, G. Gao, S. Ding, Z. Yang, W. Yu, B. Q. Li, *Electrochimica Acta* **2013**, *98*, 263.

[46] H. Kato, M. Sano, K. Miyamoto, T. Yao, *J. Cryst. Growth* **2002**, *237*, 538.

[47] M. Morana, P. Koers, C. Waldauf, M. Koppe, D. Muehlbacher, P. Denk, M. Scharber, D. Waller, C. Brabec, *Adv. Funct. Mater.* **2007**, *17*, 3274.

[48] P. Becker, J. A. Márquez, J. Just, A. Al-Ashouri, C. Hages, H. Hempel, M. Jošt, S. Albrecht, R. Frahm, T. Unold, *Adv. Energy Mater.* **2019**, *9*, 1900555.

[49] H. Choi, J. Jeong, H.-B. Kim, S. Kim, B. Walker, G.-H. Kim, J. Y. Kim, *Nano Energy* **2014**, *7*, 80.

[50] G. E. Eperon, G. M. Paternò, R. J. Sutton, A. Zampetti, A. A. Haghighirad, F. Cacialli, H. J. Snaith, *J. Mater. Chem. A,* **2015**, *3*, 19688.

[51] Y. Hu, Q. Xu, W. Ruan, S. Zhang, C. Yang, Z. Yan, F. Xu, *Solar RRL* **2019**, *3*, 1900287.

[52] B. Li, Y. Zhang, L. Fu, T. Yu, S. Zhou, L. Zhang, L. Yin, *Nat. Commun.* **2018**, *9*, 1076.

[53] Q. Wang, X. Zheng, Y. Deng, J. Zhao, Z. Chen, J. Huang, *Joule* **2017**, *1*, 371.

[54] Y. Hu, F. Bai, X. Liu, Q. Ji, X. Miao, T. Qiu, S. Zhang, *ACS Energy Lett.* **2017**, *2*, 2219.

[55] F. Liu, C. Ding, Y. Zhang, T. S. Ripolles, T. Kamisaka, T. Toyoda, S. Hayase, T. Minemoto, K.

Yoshino, S. Dai, M. Yanagida, H. Noguchi, Q. Shen, *J. Am. Chem. Soc.* **2017**, *139*, 16708.

[56] Z. Du, D. Fu, T. Yang, Z. Fang, W. Liu, F. Gao, L. Wang, Z. Yang, J. Teng, H. Zhang, W. Yang, *J, Mater. Chem. C* **2018**, *6*, 6287.

[57] C. F. J. Lau, X. Deng, J. Zheng, J. Kim, Z. Zhang, M. Zhang, J. Bing, B. Wilkinson, L. Hu, R. Patterson, S. Huang, A. Ho-Baillie, *J. Mater. Chem. A* **2018**, *6*, 5580.

[58] Q. A. Akkerman, D. Meggiolaro, Z. Dang, F. De Angelis, L. Manna, *ACS Energy Lett.* **2017**, *2*, 2183.

[59] A. K. Jena, A. Kulkarni, Y. Sanehira, M. Ikegami, T. Miyasaka, *Chem. Mater.* **2018**, *30*, 6668.

[60] S. Xiang, W. Li, Y. Wei, J. Liu, H. Liu, L. Zhu, H. Chen, *Nanoscale* **2018**, *10*, 9996.

[61] S. Xiang, W. Li, Y. Wei, J. Liu, H. Liu, L. Zhu, S. Yang, H. Chen, *iScience* **2019**, *15*, 156.

[62] T. Zhang, M. I. Dar, G. Li, F. Xu, N. Guo, M. Grätzel, Y. Zhao, *Sci. Adv.* **2017**, *3*, e1700841.

[63] Y. Jiang, J. Yuan, Y. Ni, J. Yang, Y. Wang, T. Jiu, M. Yuan, J. Chen, *Joule* **2018**, *2*, 1356.

[64] P. Wang, X. Zhang, Y. Zhou, Q. Jiang, Q. Ye, Z. Chu, X. Li, X. Yang, Z. Yin, J. You, *Nat. Commun.* **2018**, *9*, 2225.

[65] Y. Wang, T. Zhang, M. Kan, Y. Zhao, *J. Am. Chem. Soc.* **2018**, *140*, 12345.

[66] Y. Wang, T. Zhang, M. Kan, Y. Li, T. Wang, Y. Zhao, *Joule* **2018**, *2*, 2065.

[67] K. Wang, Z. Jin, L. Liang, H. Bian, D. Bai, H. Wang, J. Zhang, Q. Wang, S. Liu, *Nat. Commun.* **2018**, *9*, 4544.

[68] Y. Wang, M. I. Dar, L. K. Ono, T. Zhang, M. Kan, Y. Li, L. Zhang, X. Wang, Y. Yang, X. Gao, Y. Qi, M. Grätzel, Y. Zhao, *Science* **2019**, *365*, 591.

[69] M. Kulbak, D. Cahen, G. Hodes, *J. Phys. Chem. Lett.* **2015**, *6*, 2452.

[70] M. Kulbak, S. Gupta, N. Kedem, I. Levine, T. Bendikov, G. Hodes, D. Cahen, *J. Phys. Chem. Let.*

2016, *7*, 167.

[71] X. Chang, W. Li, L. Zhu, H. Liu, H. Geng, S. Xiang, J. Liu, H. Chen, *ACS Appl. Mater. Inter.* **2016**, *8*, 33649.

[72] J. Liang, C. Wang, Y. Wang, Z. Xu, Z. Lu, Y. Ma, H. Zhu, Y. Hu, C. Xiao, X. Yi, G. Zhu, H. Lv, L. Ma, T. Chen, Z. Tie, Z. Jin, J. Liu, *J. Am. Chem. Soc.* **2016**, *138*, 15829.

[73] J. Duan, Y. Zhao, B. He, Q. Tang, *Small* **2018**, *14*, e1704443.

[74] J. Duan, Y. Zhao, B. He, Q. Tang, *Angew. Chem. Int. Ed.* **2018**, *57*, 3787.

[75] Y. Li, J. Duan, H. Yuan, Y. Zhao, B. He, Q. Tang, *Solar RRL* **2018**, *2*, 1800164.

[76] J. Duan, Y. Zhao, X. Yang, Y. Wang, B. He, Q. Tang, *Adv. Energy Mater.* **2018**, *8*, 1802346.

[77] Q. A. Akkerman, M. Gandini, F. Di Stasio, P. Rastogi, F. Palazon, G. Bertoni, J. M. Ball, M. Prato, A. Petrozza, L. Manna, *Nat. Energy* **2016**, *2*, 16194.

[78] S. Zhou, R. Tang, L. Yin, *Adv. Mater.* **2017**, *29*, 1703682.

[79] J. Ding, J. Duan, C. Guo, Q. Tang, *J. Mater. Chem. A* **2018**, *6*, 21999.

[80] J. Duan, T. Hu, Y. Zhao, B. He, Q. Tang, *Angew. Chem. Int. Ed.* **2018**, *57*, 5746.

[81] Y. Zhao, J. Duan, H. Yuan, Y. Wang, X. Yang, B. He, Q. Tang, *Solar RRL* **2019**, *3*, 1800284.

[82] H. Xu, J. Duan, Y. Zhao, Z. Jiao, B. He, Q. Tang, *J. Power Sources* **2018**, *399*, 76.

[83] J. Duan, Y. Zhao, Y. Wang, X. Yang, Q. Tang, *Angew. Chem. Int. Ed.* **2019**, *58*, 16147.

[84] C.-X. Qian, Z.-Y. Deng, K. Yang, J. Feng, M.-Z. Wang, Z. Yang, S. Liu, H.-J. Feng, *Appl. Phys. Lett.* **2018**, *112*, 093901.

[85] H. Li, G. Tong, T. Chen, H. Zhu, G. Li, Y. Chang, L. Wang, Y. Jiang, *J. Mater. Chem. A* **2018**, *6*, 14255.

[86] D. Wang, W. Li, Z. Du, G. Li, W. Sun, J. Wu, Z. Lan, *ACS Appl. Mater. Interfaces* **2020**, *12*, 10579.

[87] W. Chen, J. Zhang, G. Xu, R. Xue, Y. Li, Y. Zhou, J. Hou, Y. Li, *Adv. Mater.* **2018**, *30*, 1800855.

[88] R. J. Sutton, G. E. Eperon, L. Miranda, E. S. Parrott, B. A. Kamino, J. B. Patel, M. T. Hörantner, M. B. Johnston, A. A. Haghighirad, D. T. Moore, H. J. Snaith, *Adv. Energy Mater.* **2016**, *6*, 1502458.

[89] R. E. Beal, D. J. Slotcavage, T. Leijtens, A. R. Bowring, R. A. Belisle, W. H. Nguyen, G. F. Burkhard, E. T. Hoke, M. D. McGehee, *J. Phys. Chem. Lett.* **2016**, *7*, 746.

[90] J. K. Nam, S. U. Chai, W. Cha, Y. J. Choi, W. Kim, M. S. Jung, J. Kwon, D. Kim, J. H. Park, *Nano Lett.* **2017**, *17*, 2028.

[91] C. F. J. Lau, M. Zhang, X. Deng, J. Zheng, J. Bing, Q. Ma, J. Kim, L. Hu, M. A. Green, S. Huang, A. Ho-Baillie, *ACS Energy Lett.* **2017**, *2*, 2319.

[92] N. Li, Z. Zhu, J. Li, A. K.-Y. Jen, L. Wang, *Adv. Energy Mater.* **2018**, *8*, 1800525.

[93] J. Liang, P. Zhao, C. Wang, Y. Wang, Y. Hu, G. Zhu, L. Ma, J. Liu, Z. Jin, *J. Am. Chem. Soc.* **2017**, *139*, 14009.

[94] J. Liang, Z. Liu, L. Qiu, Z. Hawash, L. Meng, Z. Wu, Y. Jiang, L. K. Ono, Y. Qi, *Adv. Energy Mater.* **2018**, *8*, 1800504.

[95] D. Bai, J. Zhang, Z. Jin, H. Bian, K. Wang, H. Wang, L. Liang, Q. Wang, S. F. Liu, *ACS Energy Lett.* **2018**, *3*, 970.

[96] W. Xiang, Z. Wang, D. J. Kubicki, W. Tress, J. Luo, D. Prochowicz, S. Akin, L. Emsley, J. Zhou, G. Dietler, M. Grätzel, A. Hagfeldt, *Joule* **2019**, *3*, 205.

[97] C. Liu, W. Li, H. Li, H. Wang, C. Zhang, Y. Yang, X. Gao, Q. Xue, H.-L. Yip, J. Fan, R. E. I. Schropp, Y. Mai, *Adv. Energy Mater.* **2019**, *9*, 1803572.

[98] J. Liang, X. Han, J. H. Yang, B. Zhang, Q. Fang, J. Zhang, Q. Ai, M. M. Ogle, T. Terlier, A. A. Martí, J. Lou, *Adv. Mater.* **2019**, *31*, 1903448.

[99] K. L. Wang, R. Wang, Z. K. Wang, M. Li, Y. Zhang, H. Ma, L. S. Liao, Y. Yang, *Nano Lett.* **2019**, *19*, 5176.

[100] F. Yang, D. Hirotani, G. Kapil, M. A. Kamarudin, C. H. Ng, Y. Zhang, Q. Shen, S. Hayase, *Angew. Chem. Int. Ed.* **2018**, *57*, 12745.

[101] W. S. Subhani, K. Wang, M. Du, S. F. Liu, *Nano Energy* **2019**, *61*, 165.

[102] J. Lu, S.-C. Chen, Q. Zheng, *Sci. China Chem.* **2019**, *62*, 1044.

[103] H. Sun, J. Zhang, X. Gan, L. Yu, H. Yuan, M. Shang, C. Lu, D. Hou, Z. Hu, Y. Zhu, L. Han, *Adv. Energy Mater.* **2019**, *9*, 1900896.

[104] W. Xiang, Z. Wang, D. J. Kubicki, X. Wang, W. Tress, J. Luo, J. Zhang, A. Hofstetter, L. Zhang, L. Emsley, M. Gratzel, A. Hagfeldt, *Nat. Commun.* **2019**, *10*, 4686.

[105] L. Yan, Q. Xue, M. Liu, Z. Zhu, J. Tian, Z. Li, Z. Chen, Z. Chen, H. Yan, H.-L. Yip, Y. Cao, *Adv. Mater.* **2018**, *30*, 1802509.

[106] Z. Li, R. Wang, J. Xue, X. Xing, C. Yu, T. Huang, J. Chu, K. L. Wang, C. Dong, Z. Wei, Y. Zhao, Z. K. Wang, Y. Yang, *J. Am. Chem. Soc.* **2019**, *141*, 17610.

[107] Q. Zeng, X. Zhang, X. Feng, S. Lu, Z. Chen, X. Yong, S. A. T. Redfern, H. Wei, H. Wang, H. Shen, W. Zhang, W. Zheng, H. Zhang, J. S. Tse, B. Yang, *Adv. Mater.* **2018**, *30*, 1705393.

[108] C. Liu, W. Li, C. Zhang, Y. Ma, J. Fan, Y. Mai, *J. Am. Chem. Soc.* **2018**, *140*, 3825.

[109] Q. Ye, Y. Zhao, S. Mu, F. Ma, F. Gao, Z. Chu, Z. Yin, P. Gao, X. Zhang, J. You, *Adv. Mater.* **2019**, e1905143.

[110] L. Fu, Y. Nie, B. Li, N. Li, B. Cao, L. Yin, *Solar RRL* **2019**, *3*, 1900233.

[111] S. Yang, Z. Guo, L. Gao, F. Yu, C. Zhang, M. Fan, G. Wei, T. Ma, *Solar RRL* **2019**, *3*, 1900212.

[112] J. Wang, J. Zhang, Y. Zhou, H. Liu, Q. Xue, X. Li, C. C. Chueh, H. L. Yip, Z. Zhu, A. K. Y. Jen,

Nat. Commun. **2020**, *11*, 177.

[113] Y. Zhang, C. Wu, D. Wang, Z. Zhang, X. Qi, N. Zhu, G. Liu, X. Li, H. Hu, Z. Chen, L. Xiao, B. Qu, *Solar RRL* **2019**, 1900254.

[114] B. Zhang, W. Bi, Y. Wu, C. Chen, H. Li, Z. Song, Q. Dai, L. Xu, H. Song, *ACS Appl. Mater. Interfaces* **2019**, *11*, 33868.

[115] C. Dong, X. Han, Y. Zhao, J. Li, L. Chang, W. Zhao, *Solar RRL* **2018**, *2*, 1800139.

[116] J. Zhang, Z. Jin, L. Liang, H. Wang, D. Bai, H. Bian, K. Wang, Q. Wang, N. Yuan, J. Ding, S. F. Liu, *Adv. Sci.* **2018**, *5*, 1801123.

[117] H. Bian, D. Bai, Z. Jin, K. Wang, L. Liang, H. Wang, J. Zhang, Q. Wang, S. Liu, *Joule* **2018**, *2*, 1500.

[118] J. Tian, Q. Xue, X. Tang, Y. Chen, N. Li, Z. Hu, T. Shi, X. Wang, F. Huang, C. J. Brabec, H. L. Yip, Y. Cao, *Adv. Mater.* **2019**, *31*, e1901152.

[119] W. Chen, H. Chen, G. Xu, R. Xue, S. Wang, Y. Li, Y. Li, *Joule* **2019**, *3*, 191.

[120] Q. Ma, S. Huang, S. Chen, M. Zhang, C. F. J. Lau, M. N. Lockrey, H. K. Mulmudi, Y. Shan, J. Yao, J. Zheng, X. Deng, K. Catchpole, M. A. Green, A. W. Y. Ho-Baillie, *J. Phys. Chem. C* **2017**, *121*, 19642.

[121] X. Meng, Z. Wang, W. Qian, Z. Zhu, T. Zhang, Y. Bai, C. Hu, S. Xiao, Y. Yang, S. Yang, *J. Phys. Chem. Lett.* **2019**, *10*, 194.

[122] Q. Guo, Y. Bai, K. Lang, Z. Z. Yu, T. Hayat, A. Alsaedi, E. Zhou, Z. Tan, *ACS Appl. Mater. Interfaces* **2019**, *11*, 37991.

[123] F. Guo, S. Qiu, J. Hu, H. Wang, B. Cai, J. Li, X. Yuan, X. Liu, K. Forberich, C. J. Brabec, Y. Mai, *Adv. Sci.* **2019**, *6*, 1901067.

[124] F. Guo, W. He, S. Qiu, C. Wang, X. Liu, K. Forberich, C. J. Brabec, Y. Mai, *Adv. Funct. Mater.* **2019**, *29*, 1900964.

[125] C. F. J. Lau, X. Deng, Q. Ma, J. Zheng, J. S. Yun, M. A. Green, S. Huang, A. W. Y. Ho-Baillie, *ACS Energy Lett.* **2016**, *1*, 573.

[126] Y. Fan, J. Fang, X. Chang, M.-C. Tang, D. Barrit, Z. Xu, Z. Jiang, J. Wen, H. Zhao, T. Niu, D.-M. Smilgies, S. Jin, Z. Liu, E. Q. Li, A. Amassian, S. Liu, K. Zhao, *Joule* **2019**, *3*, 2485.

[127] G. Grancini, C. Roldán-Carmona, I. Zimmermann, E. Mosconi, X. Lee, D. Martineau, S. Narbey, F. Oswald, F. De Angelis, M. Graetzel, M. K. Nazeeruddin, *Nat. Commun.* **2017**, *8*, 15684.

[128] N. Wang, Y. Zhou, M.-G. Ju, H. F. Garces, T. Ding, S. Pang, X. C. Zeng, N. P. Padture, X. W. Sun, *Adv. Energy Mater.* **2016**, *6*, 1601130.

[129] K. P. Marshall, M. Walker, R. I. Walton, R. A. Hatton, *Nature Energy* **2016**, *1*, 16178.

[130] J. H. Heo, J. Kim, H. Kim, S. H. Moon, S. H. Im, K. H. Hong, *J. Phys. Chem. Lett.* **2018**, *9*, 6024.

[131] T.-B. Song, T. Yokoyama, S. Aramaki, M. G. Kanatzidis, *ACS Energy Lett.* **2017**, *2*, 897.

[132] M. Chen, M. G. Ju, H. F. Garces, A. D. Carl, L. K. Ono, Z. Hawash, Y. Zhang, T. Shen, Y. Qi, R. L. Grimm, D. Pacifici, X. C. Zeng, Y. Zhou, N. P. Padture, *Nat. Commun.* **2019**, *10*, 16.

[133] L.-J. Chen, C.-R. Lee, Y.-J. Chuang, Z.-H. Wu, C. Chen, *J. Phys. Chem. Lett.* **2016**, *7*, 5028.

[134] S. Gupta, T. Bendikov, G. Hodes, D. Cahen, *ACS Energy Lett.* **2016**, *1*, 1028.

[135] T.-B. Song, T. Yokoyama, C. C. Stoumpos, J. Logsdon, D. H. Cao, M. R. Wasielewski, S. Aramaki, M. G. Kanatzidis, *J. Am. Chem. Soc.* **2017**, *139*, 836.

[136] D. Sabba, H. K. Mulmudi, R. R. Prabhakar, T. Krishnamoorthy, T. Baikie, P. P. Boix, S. Mhaisalkar, N. Mathews, *J. Phys. Chem. C* **2015**, *119*, 1763.

[137] D. Moghe, L. Wang, C. J. Traverse, A. Redoute, M. Sponseller, P. R. Brown, V. Bulović, R. R. Lunt, *Nano Energy* **2016**, *28*, 469.

[138] W. Li, J. Li, J. Li, J. Fan, Y. Mai, L. Wang, *J. Mater. Chem. A* **2016**, *4*, 17104.

[139] W. Ming, H. Shi, M.-H. Du, *J. Mater. Chem. A* **2016**, *4*, 13852.

[140] T. Krishnamoorthy, H. Ding, C. Yan, W. L. Leong, T. Baikie, Z. Zhang, M. Sherburne, S. Li, M. Asta, N. Mathews, S. G. Mhaisalkar, *J. Mater. Chem. A* **2015**, *3*, 23829.

[141] B. Lee, A. Krenselewski, S. I. Baik, D. N. Seidman, R. P. H. Chang, *Sustainable Energy & Fuels* **2017**, *1*, 710.

[142] M. Chen, M.-G. Ju, A. D. Carl, Y. Zong, R. L. Grimm, J. Gu, X. C. Zeng, Y. Zhou, N. P. Padture, *Joule* **2018**, *2*, 558.

[143] C. Zhang, L. Gao, S. Teo, Z. Guo, Z. Xu, S. Zhao, T. Ma, *Sustainable Energy & Fuels* **2018**, *2*, 2419.

[144] F. Igbari, R. Wang, Z. K. Wang, X. J. Ma, Q. Wang, K. L. Wang, Y. Zhang, L. S. Liao, Y. Yang, *Nano Lett.* **2019**, *19*, 2066.

[145] F. Bai, Y. Hu, Y. Hu, T. Qiu, X. Miao, S. Zhang, *Solar Energy Materials and Solar Cells* **2018**, *184*, 15.

[146] A. Singh, K. M. Boopathi, A. Mohapatra, Y. F. Chen, G. Li, C. W. Chu, *ACS Appl. Mater. Interfaces* **2018**, *10*, 2566.

[147] E. Greul, Michiel L. Petrus, A. Binek, P. Docampo, T. Bein, *J. Mater. Chem. A* **2017**, *5*, 19972.

[148] M. Wang, P. Zeng, S. Bai, J. Gu, F. Li, Z. Yang, M. Liu, *Solar RRL* **2018**, *2*, 1800217.

[149] J. Xu, J. B. Liu, B. X. Liu, B. Huang, *J. Phys. Chem. Lett.* **2017**, *8*, 4391.

[150] Y. Jiang, H. Zhang, X. Qiu, B. Cao, *Mater. Lett.* **2017**, *199*, 50.

[151] J. M. Ball, A. Petrozza, *Nat. Energy* **2016**, *1*, 1.

[152] M. Yue, J. Su, P. Zhao, Z. Lin, J. Zhang, J. Chang, Y. Hao, *Nano-Micro Lett.* **2019**, *11*, 91.

[153] T. Liu, K. Chen, Q. Hu, R. Zhu, Q. Gong, *Adv. Energy Mater.* **2016**, *6*, 1600457.

[154] L. Meng, J. You, T.-F. Guo, Y. Yang, *Acc. Chem. Res.* **2015**, *49*, 155.

[155] W. Yan, S. Ye, Y. Li, W. Sun, H. Rao, Z. Liu, Z. Bian, C. Huang, *Adv. Energy Mater.* **2016**, *6*, 1600474.

[156] A. A. Said, J. Xie, Q. Zhang, *Small* **2019**, *15*, e1900854.

[157] Z. Chen, C. Yu, K. Shum, J. J. Wang, W. Pfenninger, N. Vockic, J. Midgley, J. T. Kenney, *J. Lumin.* **2012**, *132*, 345.

[158] H. Yuan, Y. Zhao, J. Duan, Y. Wang, X. Yang, Q. Tang, *J. Mater. Chem. A* **2018**, *6*, 24324.

[159] Q. Zeng, X. Zhang, C. Liu, T. Feng, Z. Chen, W. Zhang, W. Zheng, H. Zhang, B. Yang, *Solar RRL* **2019**, *3*, 1800239.

[160] T. Wu, Y. Wang, Z. Dai, D. Cui, T. Wang, X. Meng, E. Bi, X. Yang, L. Han, *Adv. Mater.* **2019**, *31*, 1900605.

[161] C. F. J. Lau, Z. Wang, N. Sakai, J. Zheng, C. H. Liao, M. Green, S. Huang, H. J. Snaith, A. Ho-Baillie, *Adv. Energy Mater.* **2019**, *9*, 1901685.

[162] C. Liu, Y. Yang, X. Xia, Y. Ding, Z. Arain, S. An, X. Liu, R. C. Cristina, S. Dai, M. K. Nazeeruddin, *Adv. Energy Mater.* **2020**, *10*, 1903751.

[163] Z. J. Zhou, Y. Q. Deng, P. P. Zhang, D. X. Kou, W. H. Zhou, Y. N. Meng, S. J. Yuan, S. X. Wu, *Solar RRL* **2019**, *3*, 1800354.

[164] J. Duan, Y. Wang, X. Yang, Q. Tang, *Angew. Chem. Int. Ed.* **2020**, *59*, 4391.

[165] K. C. Tang, P. You, F. Yan, *Solar RRL* **2018**, *2*, 1800075.

[166] B. Zhang, Y. Zhou, Q. Xue, J. Tian, Q. Yao, Y. Zang, L. Wang, W. Yang, H.-L. Yip, Y. Cao, *Solar RRL* **2019**, *3*, 1900265.

[167] Y. Zhou, X. Zhang, X. Lu, X. Gao, J. Gao, L. Shui, S. Wu, J. M. Liu, *Solar RRL* **2019**, *3*, 1800315.

[168] H. Wang, H. Bian, Z. Jin, L. Liang, D. Bai, Q. Wang, S. F. Liu, *Solar RRL* **2018**, *2*, 1800216.

[169] Y. Wang, T. Zhang, F. Xu, Y. Li, Y. Zhao, *Solar RRL* **2018**, *2*, 1700180.

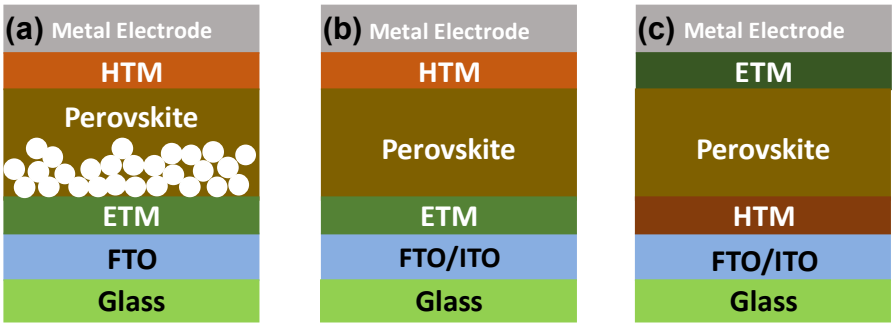


Figure 1. All-inorganic $CsBX_3$ PSCs architectures: (a) Mesoscopic, (b) Planar n-i-p (regular) heterojunction, (c) Planar p-i-n (inverted) heterojunction. HTM = hole transport material, ETM = electron transport material, FTO = fluorine doped tin oxide, ITO = indium tin oxide.

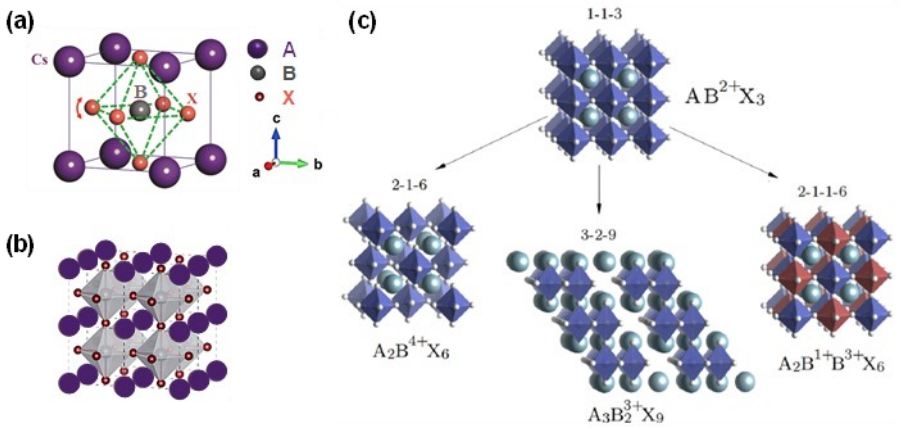


Figure 2. (a) Cubic phase structure of $CsBX_3$ perovskite. (b) Three-dimensional network structure of $CsBX_3$ perovskite. (c) Schematic relation between the crystal structures of typical and derivative $CsBX_3$ perovskites. Reproduced with permission.[10] Copyright 2016, American Chemical Society.

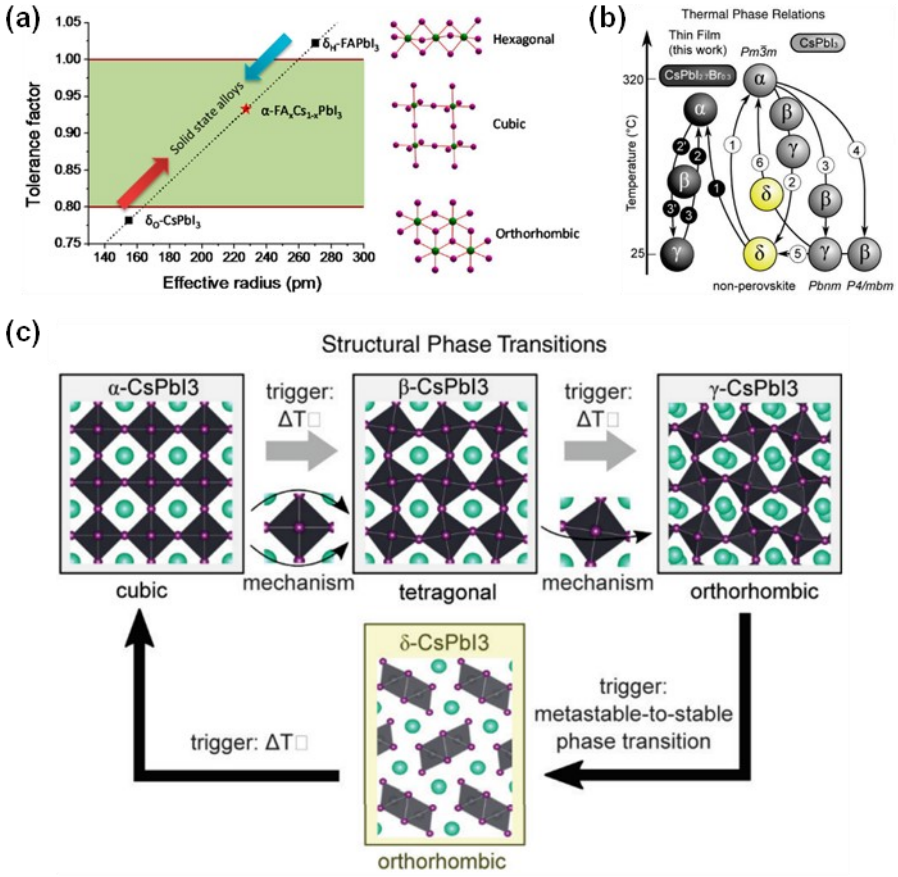


Figure 3. (a) Correlations between tolerance factor and crystal structure of perovskite materials. Reproduced with permission.[21] Copyright 2015, American Chemical Society. Polymorphic character and metastability of $CsPbI_3$: (b) Thermal phase relations of $CsPbI_3$. (c) Crystal structure of the different phases and their relative phase transitions. The transitions between the black phases are governed by the local Pb-centered octahedral (black) distortions, depicted here using one lead atom at the center and six iodide atoms at the edges (purple), confining the cesium cations (cyan). Reproduced with permission.[84] Copyright 2019, American Association for the Advancement of Science.

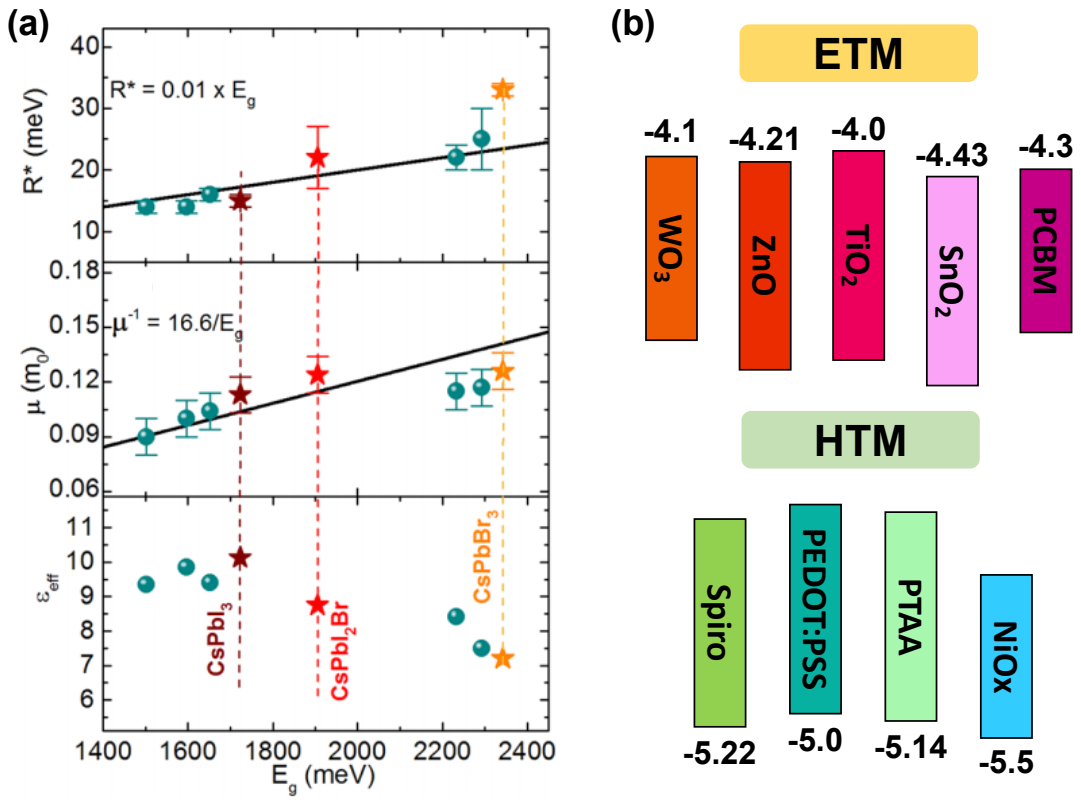


Figure 4. (a) Binding energy, effective mass and dielectric constant as a function of the band gap at 2 K. Brown, red, and yellow stars indicate the results for $CsPbI_3$, $CsPbI_2Br$, and $CsPbBr_3$, respectively. Reproduced with permission.[33] Copyright 2017, American Chemical Society. (b) The energy-band diagram of HTM and ETM in $CsBX_3$ PSCs.

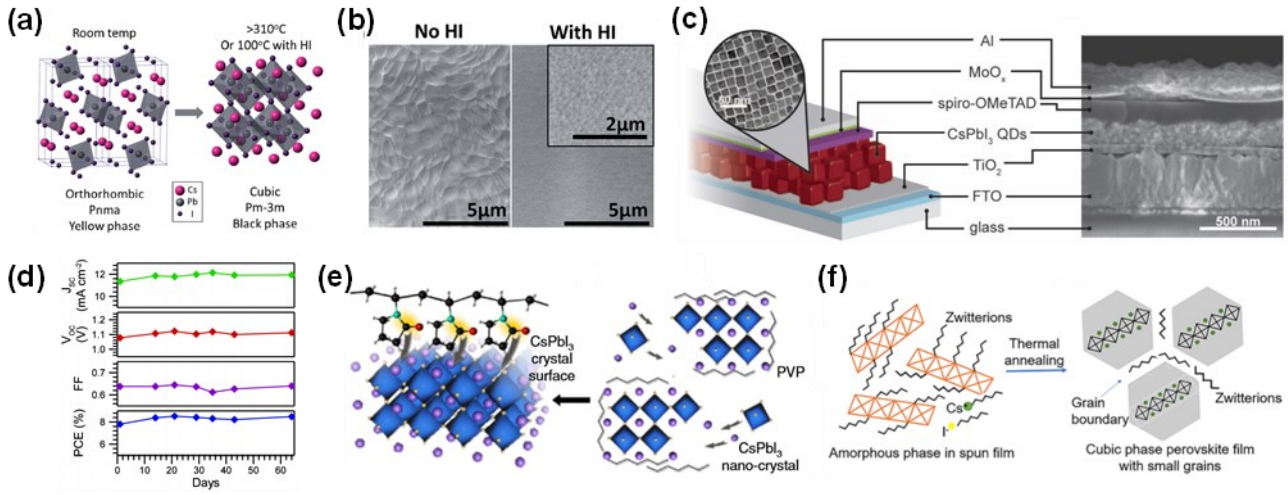


Figure 5. (a) Diagrammatic structure of $CsPbI_3$ phases. (b) Scanning electron micrographs of films fabricated with and without added HI, annealed at low and high temperatures, respectively. Reproduced with permission.[50] Copyright 2015, Royal Society of Chemistry. (c) Schematic (with TEM image of QDs) and SEM cross-section of the $CsPbI_3$ solar cell. (d) Device performance characteristics over longer time scales. A typical device was periodically measured over a 64-day time period. Performance parameters were extracted from a J-V sweep from forward bias to short-circuit. Between measurements the device was stored in the dark in a desiccator. Reproduced with permission.[8] Copyright 2016, American Association for the Advancement of Science. (e) Mechanism of PVP-induced cubic phase stability: PVP anchored at the surface of $CsPbI_3$ crystals via the combination between N/O and Cs. The negative state in $CsPbI_3$ crystals surface reduces surface tension significantly and stabilizes cubic phase. Reproduced with permission.[52] Copyright 2018, Springer Nature Publishing AG. (f) Mechanism of $CsPbI_3$ α-Phase Stabilization by Zwitterion: The zwitterion molecules are expelled toward the grain surface and GBs during $CsPbI_3$ grain growth, which maintains the small grains by impeding further grain growth. Reproduced with permission.[53] Copyright 2017, Elsevier.

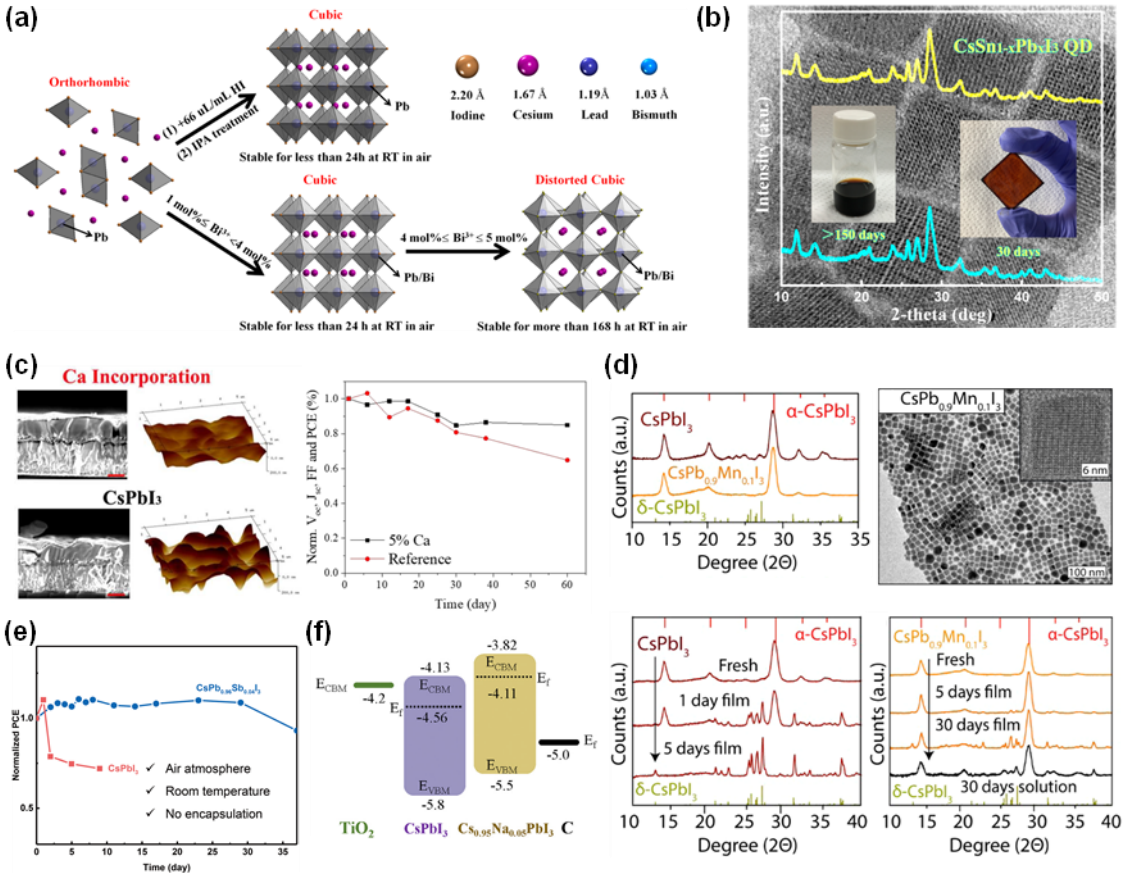


Figure 6. (a) Possible mechanisms for stabilization of α-$CsPbI_3$ by adding HI or Bi^{3+} in the precursor solution. Reproduced with permission.[54] Copyright 2017, American Chemical Society. (b) Air-stable alloyed $CsSn_{1-x}Pb_xI_3$ perovskite nanocrystals for use in solar cells. Reproduced with permission.[93] Copyright 2017, American Chemical Society. (c) Cross-sectional SEM images of perovskite devices (scale bar: 500 nm) and 3D atomic force microscope images of perovskite films using $CsPb_{0.95}Ca_{0.05}I_3$ and $CsPbI_3$ perovskite precursor solution. Normalized PCE for encapsulated $CsPb_{0.95}Ca_{0.05}I_3$ and $CsPbI_3$ devices as a function of storage time in the dark at room temperature with relative humidity between 60-70%. Reproduced with permission.[57] Copyright 2018, Royal Society of Chemistry. (d) TEM and high resolution transmission electron microscope image of $CsPb_xMn_{1-x}I_3$ NCs. And XRD pattern of $CsPbI_3$ and $CsPb_xMn_{1-x}I_3$ NCs. Reproduced with permission.[58] Copyright 2017, American Chemical Society. (e) Stability of the non-encapsulated $CsPb_{0.96}Sb_{0.04}I_3$ and $CsPbI_3$ PSCs. The devices were stored in an air atmosphere at room temperature and measured periodically in an ambient environment. Reproduced with permission.[60] Copyright 2018, Royal Society of Chemistry. (f) Energy level diagrams of $CsPbI_3$ and $Cs_{0.95}Na_{0.05}PbI_3$ PSCs. Reproduced with permission.[96] Copyright 2019, Elsevier.

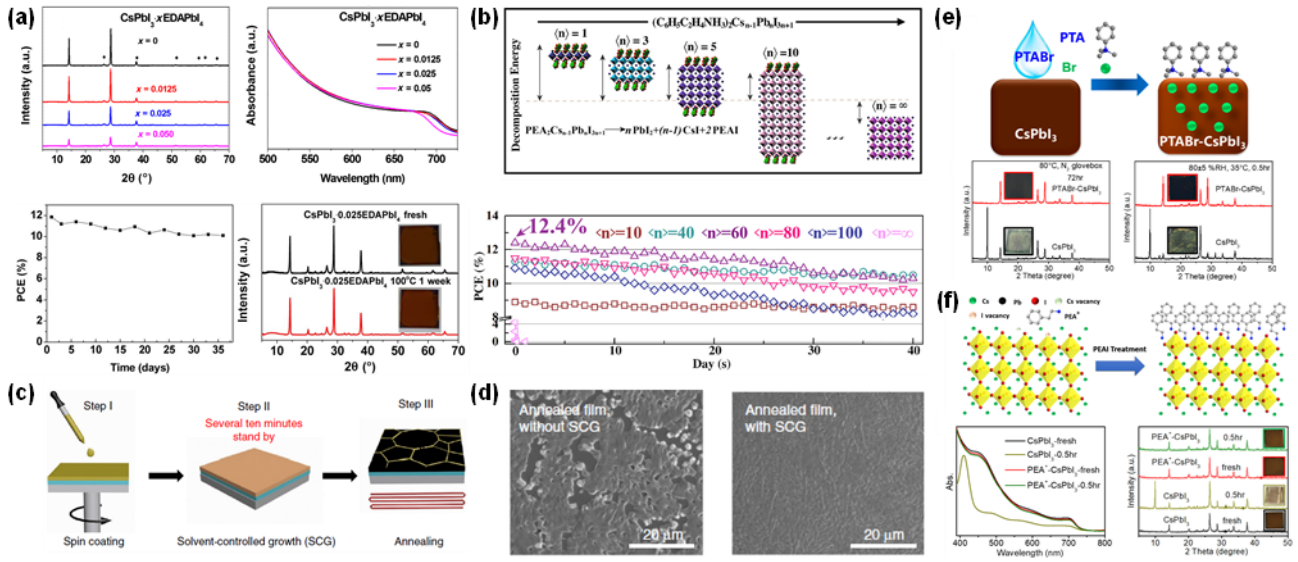


Figure 7. (a) XRD patterns and UV-vis absorption spectra of $CsPbI_3 \cdot xEDAPbI_4$ perovskites. Stability test of $CsPbI_3 \cdot 0.025EDAPbI_4$-based devices and films: PCE of the champion PSC fabricated from $CsPbI_3 \cdot 0.025EDAPbI_4$ as a function of storage time in a dark dry box; XRD pattern and images of the $CsPbI_3 \cdot 0.025EDAPbI_4$ film heated at 100°C in a dry box for 1 week. Reproduced with permission.[62] Copyright 2017, American Association for the Advancement of Science. (b) Unit cell structure of $PEA_2Cs_{n-1}Pb_nX_{3n+1}$ and decomposition energetics using first-principles density functional theory (DFT) of perovskite with different ‹n› values. And device performance evolution as a function of time under ambient atmosphere without sealing. Reproduced with permission.[63] Copyright 2018, Elsevier. (c) Schematic illustration of $CsPbI_3$-perovskite crystallization procedures via solvent-controlled growth. (d) Scanning electron microscopy images of $CsPbI_3$ perovskite film without and with solvent-controlled growth (SCG), respectively. Reproduced with permission.[64] Copyright 2018, Springer Nature Publishing AG. (e) Schematic illustration of gradient Br doping and PTA organic cation surface passivation on $CsPbI_3$ perovskite thin film. XRD patterns evolution of $CsPbI_3$ and PTABr-$CsPbI_3$ thin films at different conditions. Reproduced with permission.[65] Copyright 2018, American Chemical Society. (f) Schematic illustration of organic cation surface termination using PEAI. Moisture Stability Study of the $CsPbI_3$ and PEA^+-$CsPbI_3$ thin films when exposed to ambient environment with 85%-90% RH at RT. Reproduced with permission.[66] Copyright 2018, Elsevier.

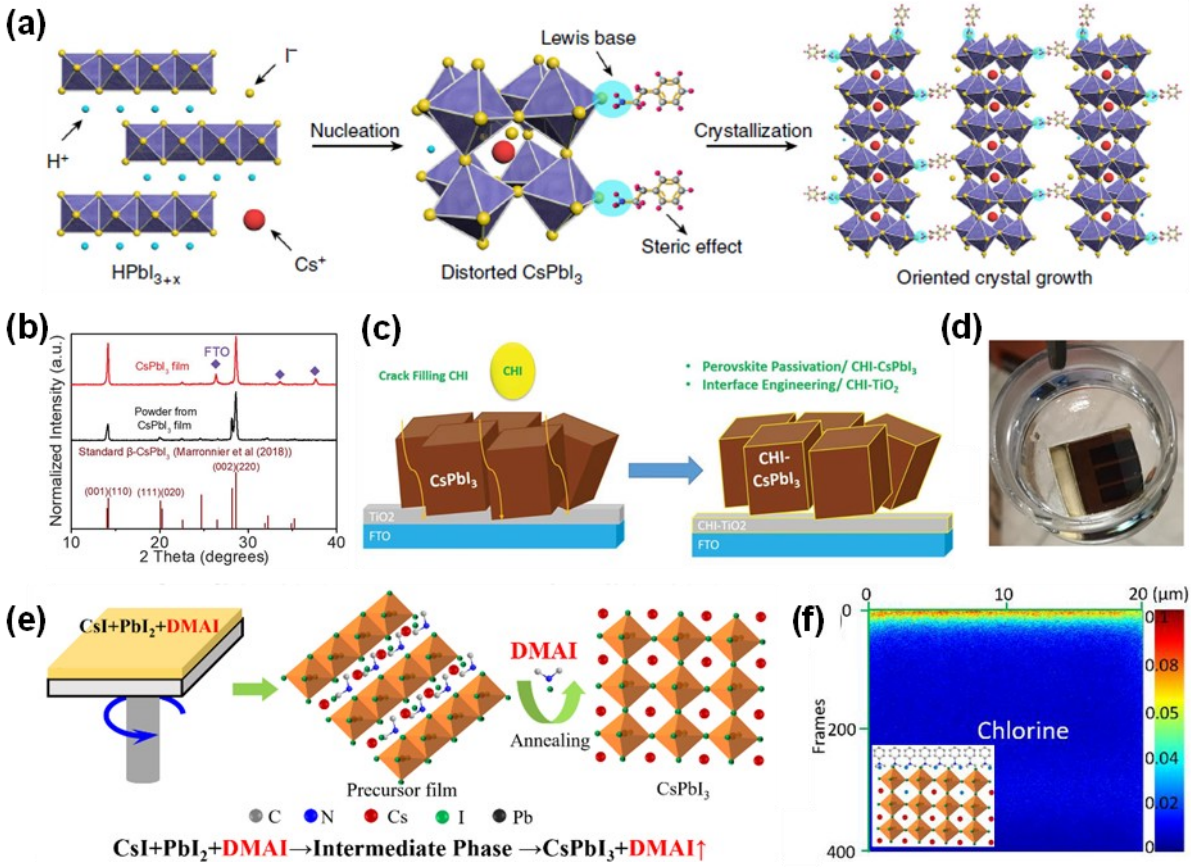


Figure 8. (a) Schematic for HI/PEAI additive-induced $CsPbI_3$ crystal growth. Reproduced with permission.[67] Copyright 2018, Springer Nature Publishing AG. (b) XRD patterns acquired from a $CsPbI_3$ thin film and powders scratched from the films. Brown lines indicate the standard β-$CsPbI_3$ XRD pattern. (c) Schematic illustration of crack-filling interface engineering. (d) Photograph of the encapsulated CHI-$CsPbI_3$ PSC device placed in water. Reproduced with permission.[99] Copyright 2019, American Association for the Advancement of Science. (e) Schematic mechanism for dimethylammonium iodine (DMAI) additive induced black phase $CsPbI_3$ formation. (f) Cross-sectional of chlorine elemental profile of PTACl-$CsPbI_3$ measured by time-of-flight secondary ion mass spectrometry. Reproduced with permission.[9] Copyright 2019, Wiley.

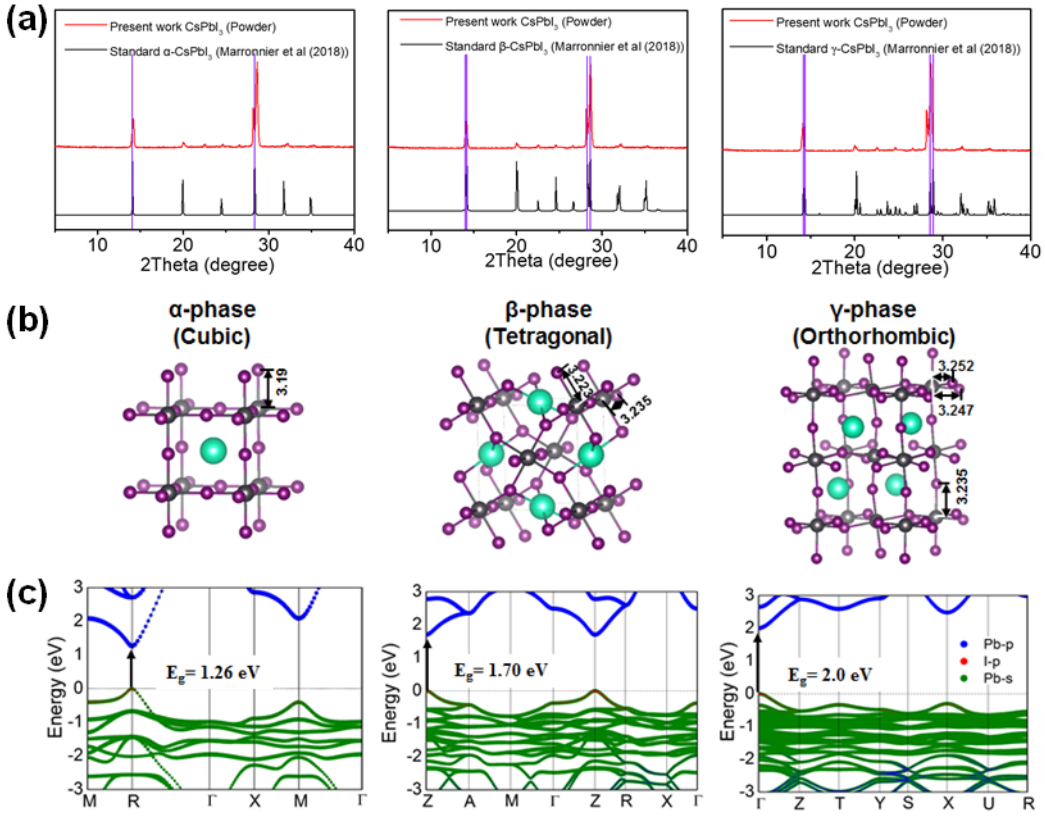


Figure 9. (a) Comparison of XRD patterns of β-$CsPbI_3$ powders scratched from a film with standard XRD patterns of α-$CsPbI_3$, β-$CsPbI_3$ and γ-$CsPbI_3$. (b) The crystal structures and (c) The band structures of α-$CsPbI_3$, β-$CsPbI_3$ and γ-$CsPbI_3$ perovskites. Theoretically optimized structural parameters were adopted. In (b) the explicit Pb-I bond lengths are indicated. In (c) the band structures are projected onto the composed atomic orbitals and the band gap values are corrected by terminology, which minimizes the band gap underestimation issue of conventional DFT calculations. Reproduced with permission.[99] Copyright 2019, American Association for the Advancement of Science.

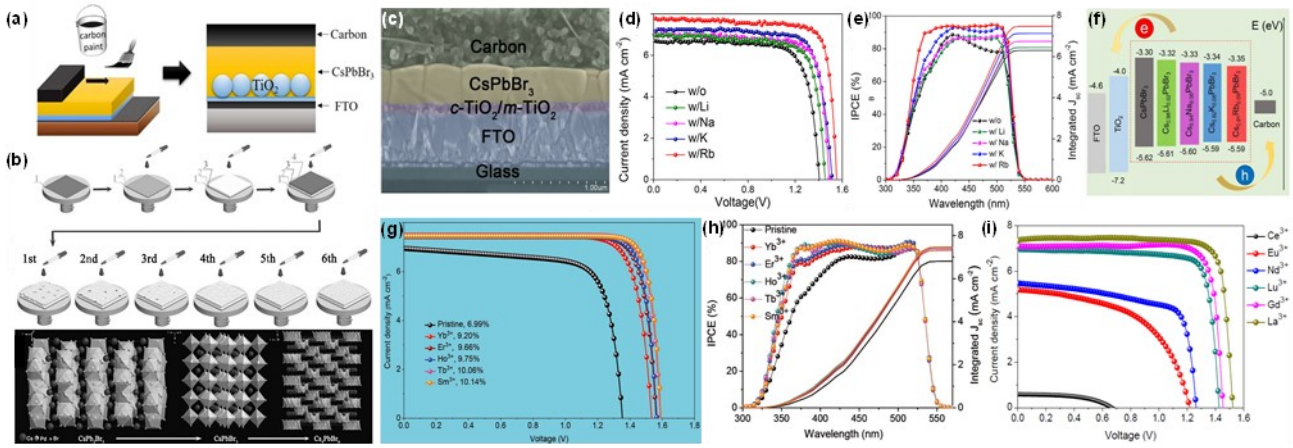


Figure 10. (a) Schematic illustration of deposition process of carbon electrode and cross-sectional structure. Reproduced with permission.[71] Copyright 2016, American Chemical Society. (b) Illustration of the deposition process on 1) FTO with 2) c-TiO_2, 3) m-TiO_2, and 4) $PbBr_2$. Multistep solution-processed deposition of CsBr. And the crystal structure conversion of the cesium lead bromide halide. Reproduced with permission.[74] Copyright 2018, Wiley. A-site lattice doping of $CsPbBr_3$ perovskite. (c) The cross-sectional SEM image of an inorganic PSC with FTO/c-TiO_2/m-TiO_2/perovskite/carbon configuration. (d) J-V curves and (e) the incident photon-to-electron conversion efficiency (IPCE) spectra of different alkali metal cations (Li^+, Na^+, K^+, Rb^+) doped $CsPbBr_3$ PSCs under AM1.5G illumination. (f) Band alignment of inorganic PSCs with $Cs_{1-x}R_xPbBr_3$ layers. Reproduced with permission.[75] Copyright 2018, Wiley. (g) J-V curves and (h) IPCE spectra of different metal cations Ln^{3+} (Sm^{3+}, Tb^{3+}, Ho^{3+}, Er^{3+}, Yb^{3+}-3% doping amount) doped $CsPbBr_3$ PSCs. (i) J-V curves of other metal cations Ln^{3+} (La^{3+}, Ce^{3+}, Nd^{3+}, Eu^{3+}, Gd^{3+}, Lu^{3+}-3% doping amount) doped $CsPbBr_3$ PSCs. Reproduced with permission.[76] Copyright 2018, Wiley.

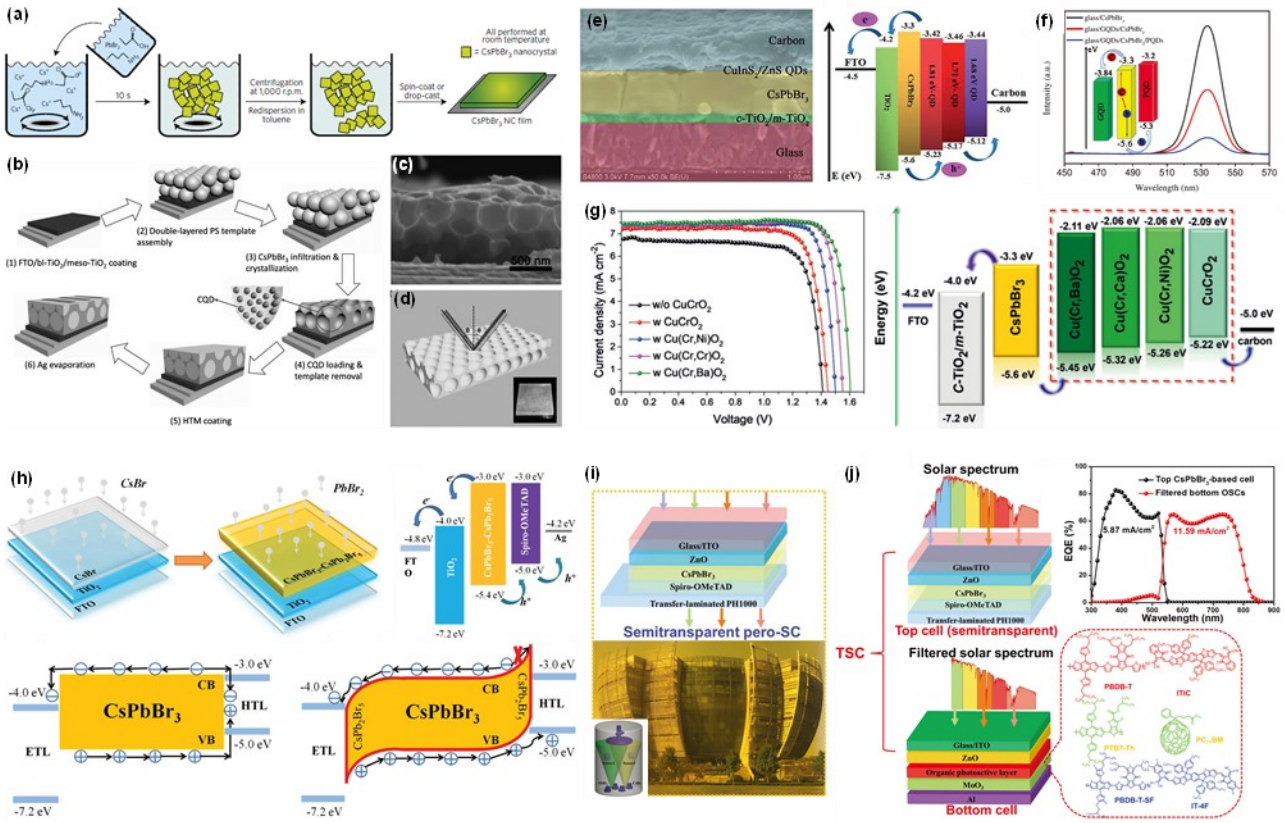


Figure 11. (a) Synthesis method of the $CsPbBr_3$ NCs passivated with short ligands, where the $PbBr_2$ precursor solution is injected in a hexane/isopropanol mixture containing Cs^+ cations. After centrifugation and redispersion in toluene, the inks can be directly used for fabrication of the films. Reproduced with permission.[77] Copyright 2016, Springer Nature Publishing AG. (b) Preparation process of CQD/$CsPbBr_3$ IO perovskite solar cells. (c) Cross-sectional SEM image of CQD/$CsPbBr_3$ IO. (d) Schematic diagram of the reflection experiment, inset is a digital photograph of $CsPbBr_3$ photonic crystal film. Reproduced with permission.[78] Copyright 2017, Wiley. (e) Cross-sectional SEM image of a total inorganic PSC device with $CuInS_2$/ZnS QDs modification and energy diagram of each layer in the device. Reproduced with permission.[79] Copyright 2018, Royal Society of Chemistry. (f) Steady-state PL spectra of glass/$CsPbBr_3$, glass/GQDs/$CsPbBr_3$, and glass/GQDs/$CsPbBr_3$/PQDs films. The inset in (f) shows the charge transfer path when inserting QD layers in solar cells. Reproduced with permission.[73] Copyright 2018, Wiley. (g) Characteristic J-V curves of various all-inorganic $CsPbBr_3$ PSCs and energy-level diagram for charge transfer process. Reproduced with permission.[83] Copyright 2019, Wiley. (h) Schematic diagram of the vapor deposition procedure for the derivative-phase inorganic perovskite film. Energy-level diagram of the inorganic PSC. Schematic diagram of the band without and with the $CsPb_2Br_5$ phase. Reproduced with permission.[85] Copyright 2018, Royal Society of Chemistry. The device structures of (i) semitransparent PSCs and (j) four-terminal TSCs: semitransparent top cell with a structure of glass/ITO/ZnO/$CsPbBr_3$/Spiro-OMeTAD/transfer-laminated PH1000; bottom OSCs with a structure of glass/ITO/ZnO/organic photoactive layer/MoO_3/Al, and molecular structures of donor and acceptor materials used in the corresponding organic photoactive layer. Reproduced with permission.[87] Copyright 2018, Wiley.

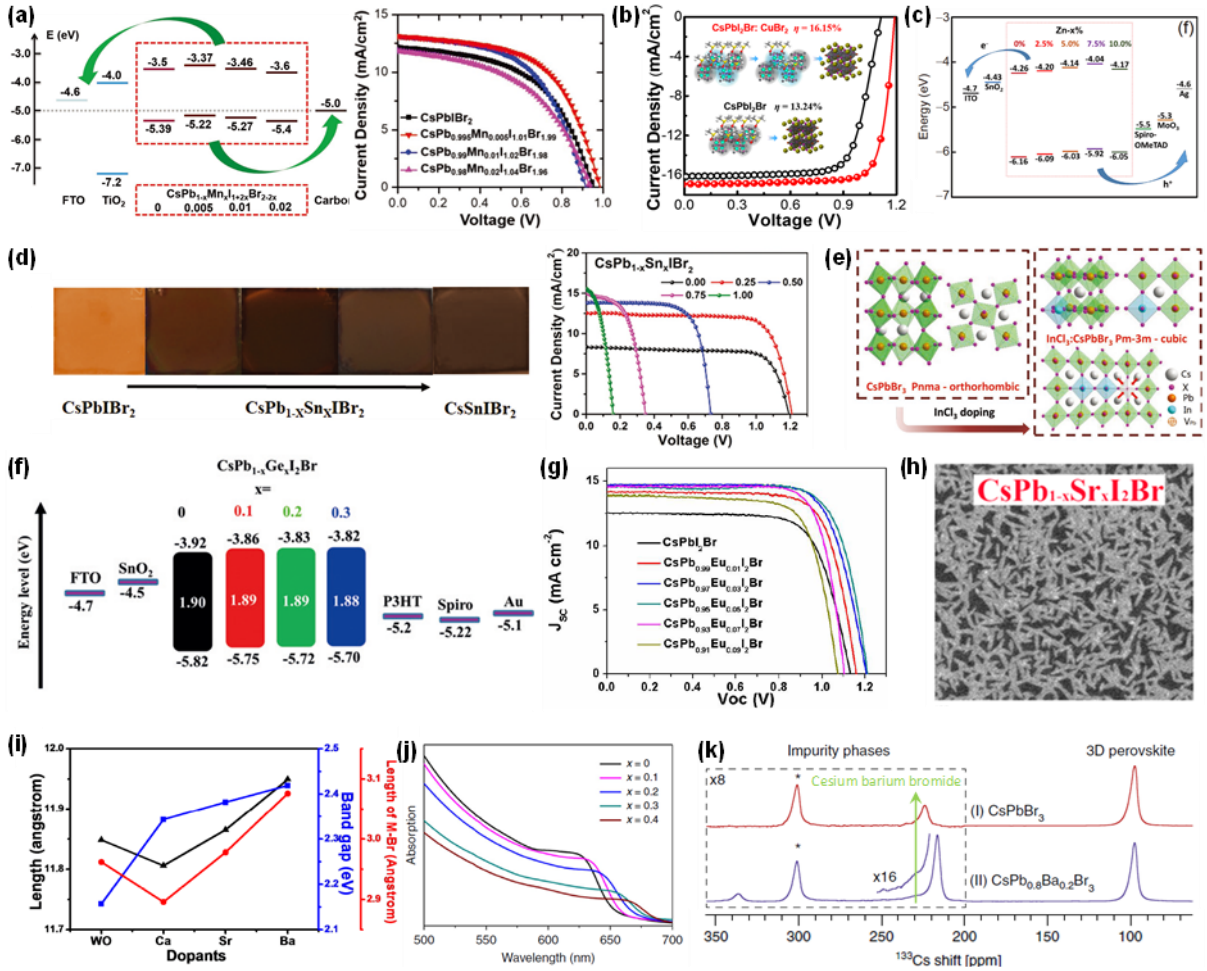


Figure 12. (a-h) Metal element doping into $CsPbI_xBr_{3-x}$ perovskite materials. Reproduced with permission.[91,92,94,96,97,99,100,102] (i) The calculated crystal lattice length of the 2×2×2 supercell, band gap and M-Br bond length as functions of dopant type. Reproduced with permission.[101] Copyright 2019, Elsevier. (j) UV-vis absorption spectra of $CsPb_{1-x}Ba_xI_2Br$ with x varies from 0 to 0.4 compositions. (k) ^{133}Cs echo-detected solid-state magic angle spinning (MAS) NMR spectra at 21.1T, 298K, and 24kHz MAS of bulk mechanochemical compositions $CsPbBr_3$ and $CsPb_{0.8}Ba_{0.2}Br_3$. Reproduced with permission.[104] Copyright 2019, Springer Nature Publishing AG.

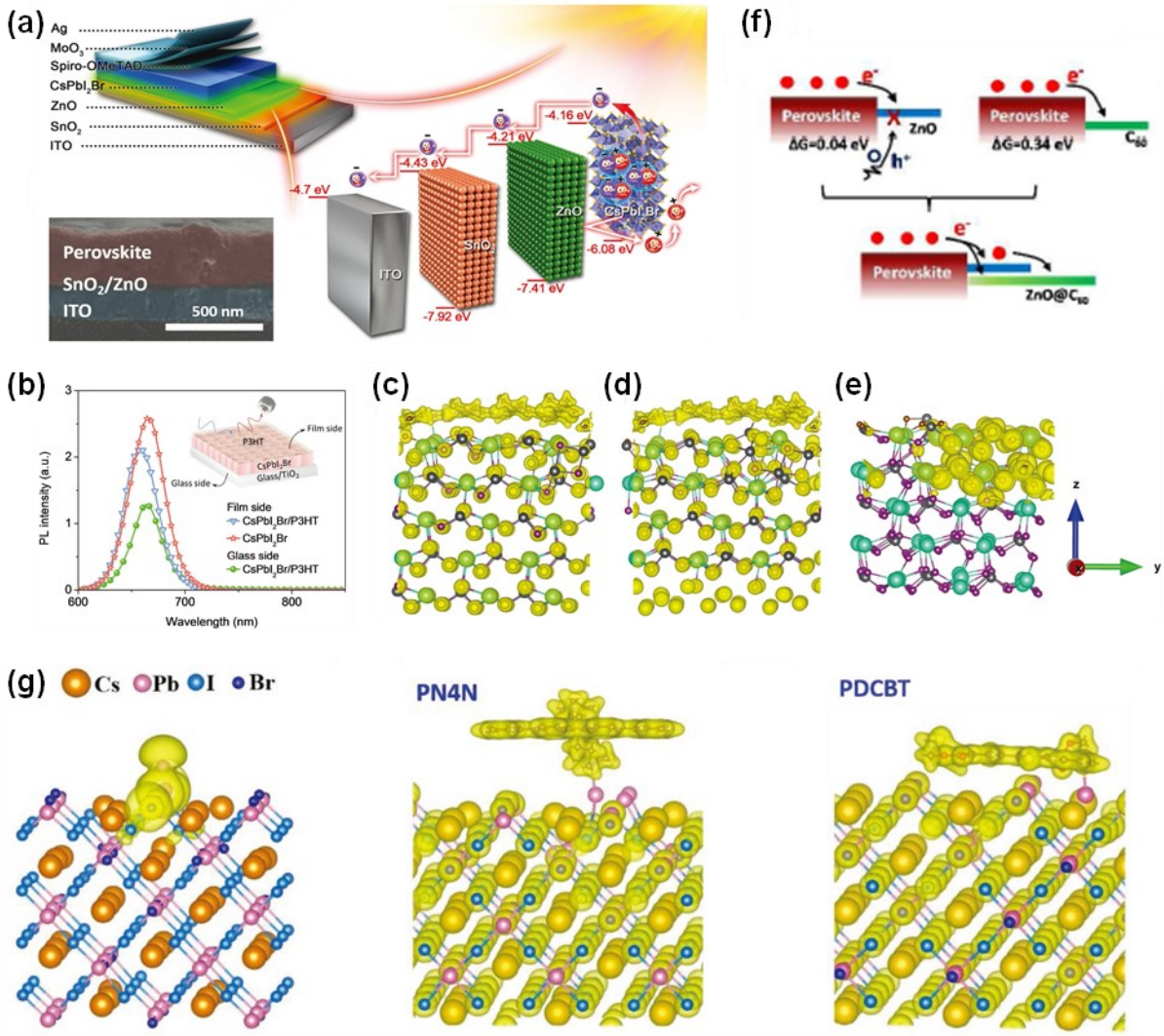


Figure 13. (a) Device architecture of the all-inorganic $CsPbI_2Br$ PSC and the corresponding energy diagrams. Reproduced with permission.[105] Copyright 2018, Wiley. Surface trap state passivation with P3HT: (b) The steady-state PL spectra for $CsPbI_2Br$ films with P3HT layer using a 405 nm laser as the excitation source from the perovskite film side, from the glass side, and $CsPbI_2Br$ films without P3HT from the perovskite film side. Inset shows the schematic of PL experiment setup. (c-e) Density distribution plots of $CsPbI_2Br$ 110-surface. (c) P3HT on 110-surface, (d) P3HT on 110-surface with antisite defects, and (e) no P3HT on 110-surface with antisite defects. Reproduced with permission.[107] Copyright 2018, Wiley. (f) Schematic view of different ETL with band-gap alignment. Reproduced with permission.[108] Copyright 2018, American Chemical Society. (g) DFT-calculated electronic configuration of $CsPbI_2Br$ surfaces and the trap state passivation effect from PN4N and PDCBT: Charge density distribution plots of $CsPbI_2Br$ (110) surface with an antisite defect and PN4N and PDCBT on $CsPbI_2Br$ (110) surface passivating the antisite defect. Reproduced with permission.[118] Copyright 2019, Wiley.

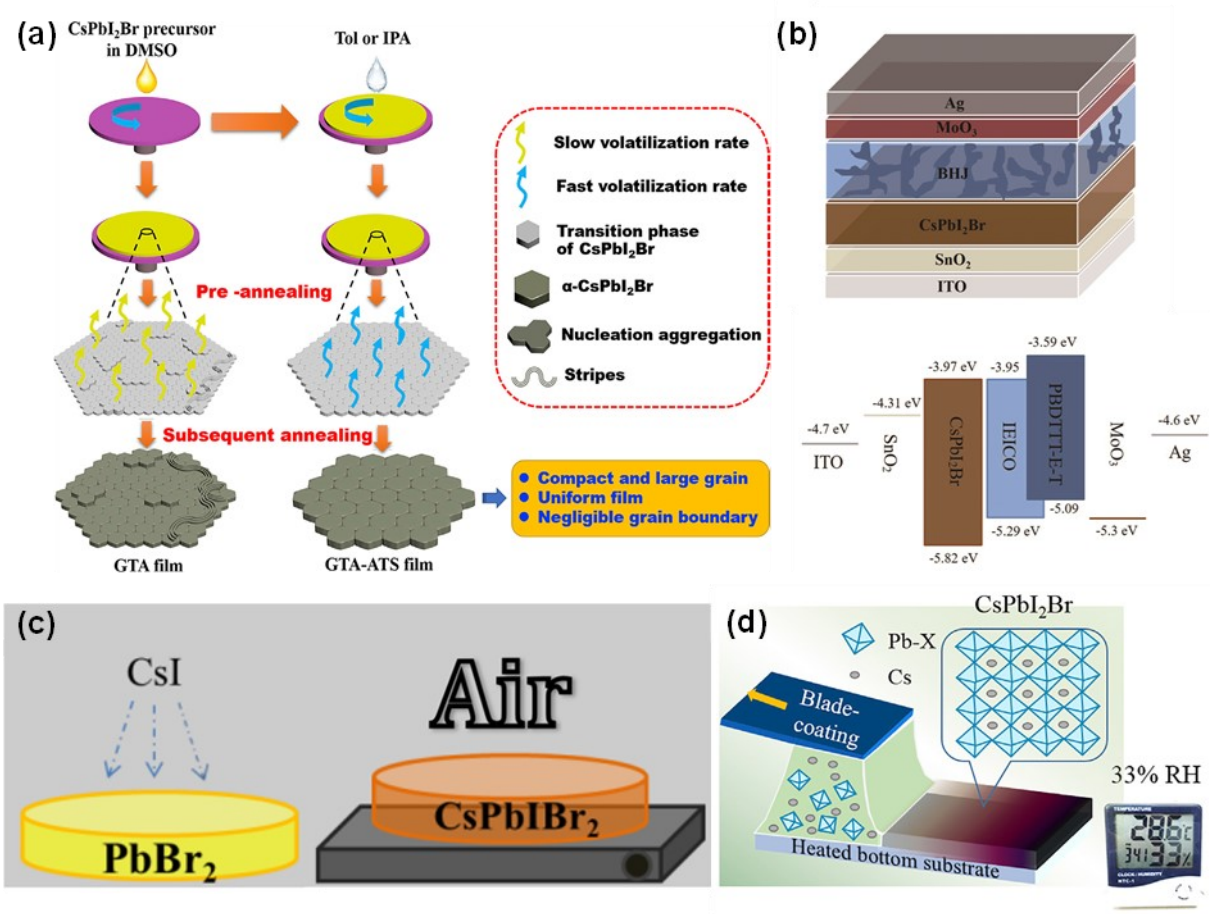


Figure 14. (a) Schematic illustration of $CsPbI_2Br$ perovskite crystallization process via GTA or GTA-ATS processing. Reproduced with permission.[119] Copyright 2018, Elsevier. (b) Device structure and electronic energy-level diagram of $CsPbI_2Br$/PBDTTT-E-T:IEICO integrated solar cells. Reproduced with permission.[122] Copyright 2019, American Chemical Society. (c) Spray-assisted deposition method for $CsPbIBr_2$ perovskite films. Reproduced with permission.[125] Copyright 2016, American Chemical Society. (d) Schematic illustration of ambient blading. Reproduced with permission.[126] Copyright 2019, Elsevier.

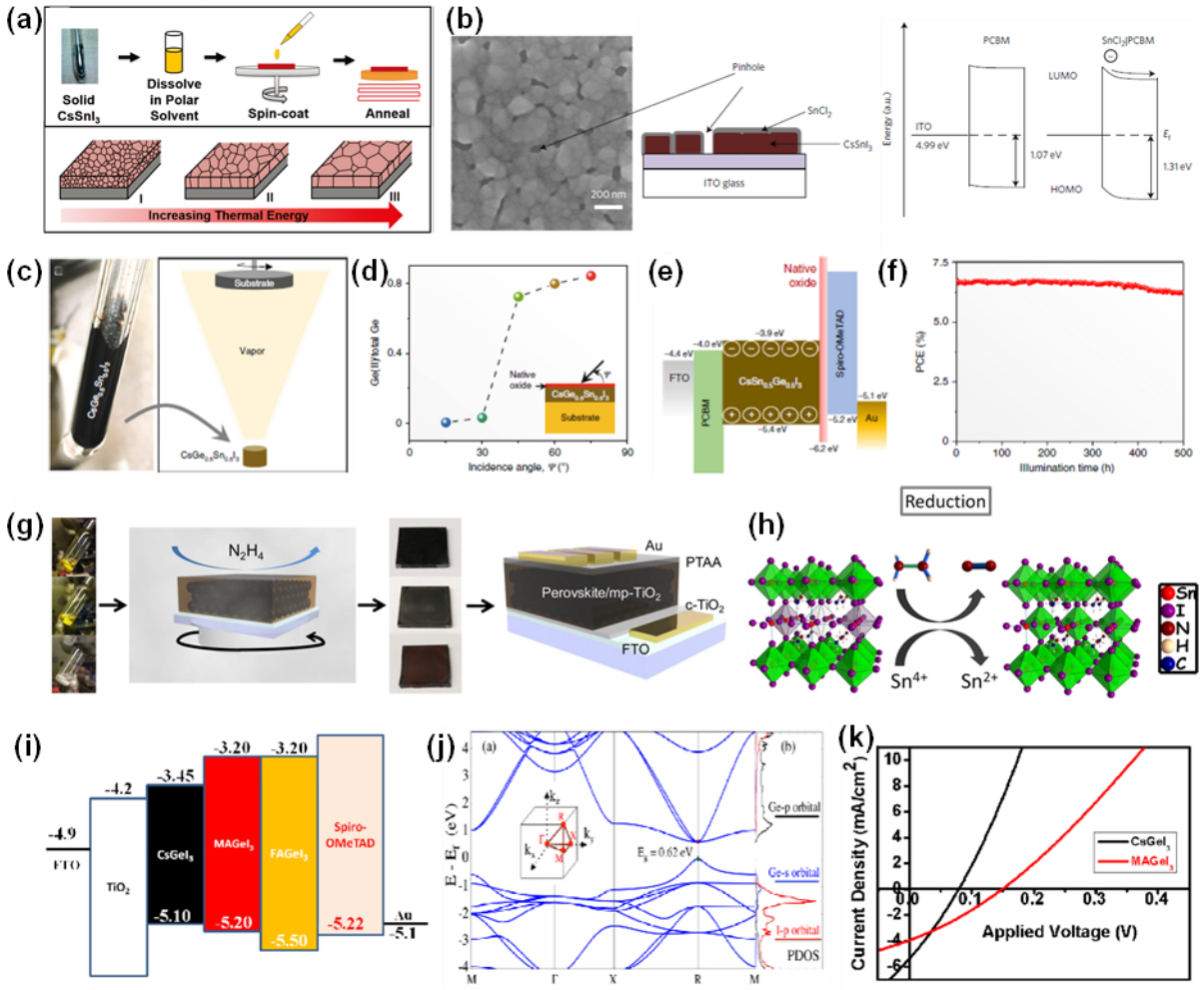


Figure 15. (a) Schematic representation of the one-step solution fabrication of B-γ-$CsSnI_3$ thin films and schematic representation of the grain-coarsening driven morphology evolution of as-deposited B-γ-$CsSnI_3$ thin film with increasing heat-treatment temperature. Reproduced with permission.[128] Copyright 2016, Wiley. (b) Schematic diagram of the proposed film structure in case $CsSnI_3$ crystallites capped with a thin $SnCl_2$ layer and energy level diagram of an ITO/$PC_{61}BM$ interface with and without $SnCl_2$. Reproduced with permission.[129] Copyright 2016, Springer Nature Publishing AG. (c) Photograph of as-synthesized $CsSn_{0.5}Ge_{0.5}I_3$ perovskite solid using the melt-crystallization method. Schematic illustration of the single-source evaporation method for the deposition of ultrasmooth $CsSn_{0.5}Ge_{0.5}I_3$ perovskite thin film. (d) The Corresponding plot of the fraction of Ge (II) in Ge 3d X-ray photoelectron spectroscopy spectra, at different incidence angles, from $CsSn_{0.5}Ge_{0.5}I_3$ perovskite thin film that has been exposed to air. (e) Energy-level diagram of $CsSn_{0.5}Ge_{0.5}I_3$ thin-film PSCs. (f) The PCE evolution of a typical unencapsulated $CsSn_{0.5}Ge_{0.5}I_3$ PSC in continuous operation under 1-sun illumination at 45°C in N_2 atmosphere. Reproduced with permission.[132] Copyright 2019, Springer Nature Publishing AG. (g) Scheme of reducing vapor atmosphere process of device fabrication. (h) Proposed possible mechanism of hydrazine vapor reaction with Sn-based perovskite materials. Reproduced with permission.[135] Copyright 2017, American Chemical Society. (i) Schematic energy level diagram of $CsGeI_3$. (j) Calculated band structure and projected density of states of $CsGeI_3$. The energy of the highest occupied state is set to 0 eV. (k) J-V curves of photovoltaic devices fabricated with $CsGeI_3$ perovskites. Reproduced with permission.[140] Copyright 2015, Royal Society of

Chemistry.

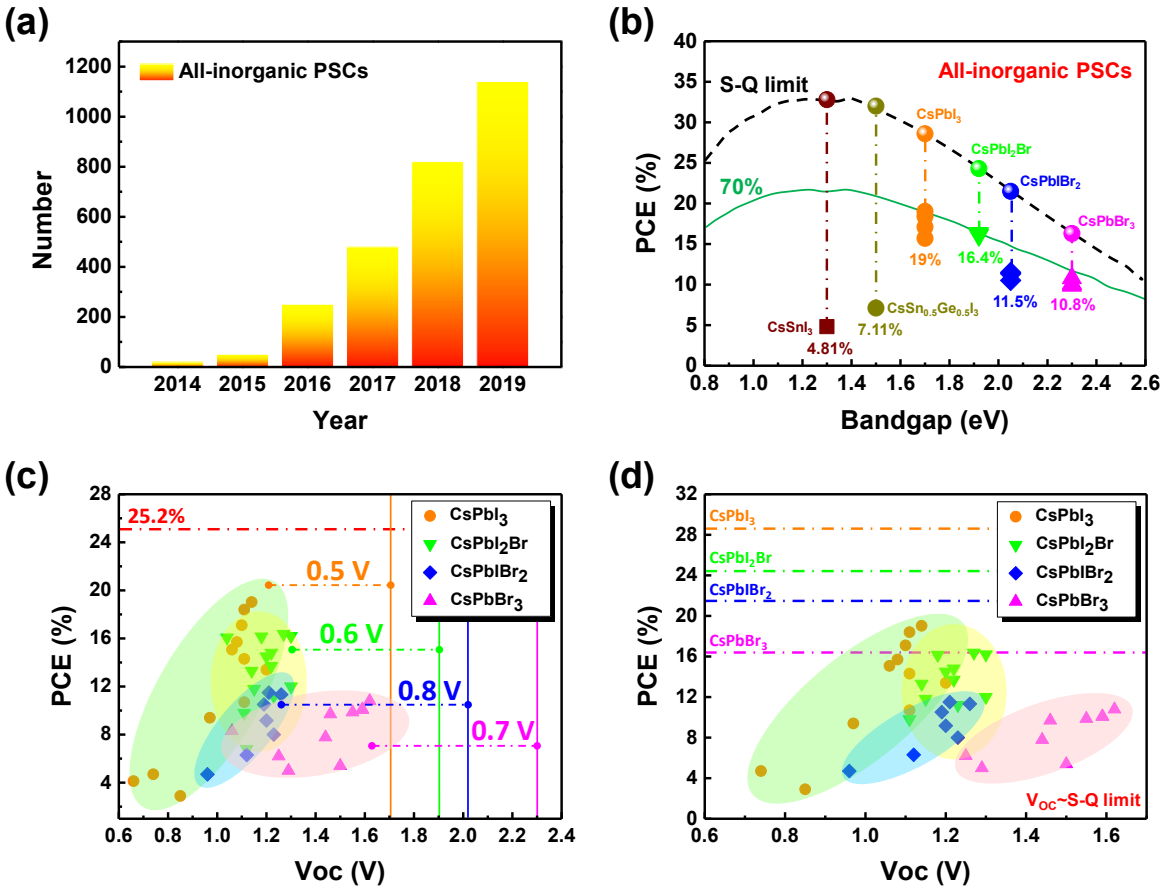


Figure 16. (a) The annual number of published periodical articles on all-inorganic perovskite solar cells. (b) The record efficiencies of all-inorganic perovskite PSCs with different bandgaps and their corresponding Shockley-Queisser efficiency limit. (c) The relationship between the PCE and the corresponding V_{OC} of the high efficiency devices based on $CsPbX_3$ PSCs. (d) The relationship between V_{OC} and the corresponding Shockley-Queisser efficiency limit of high efficiency devices based on $CsPbX_3$ PSCs.

Table 1. Effective ionic radii of commonly-used cations and anions in $CsBX_3$ perovskites

Ion group	Ion category	Coordination number	Ionic radius (Å)
A site	Cs^{+}	12	1.69
	Na^{+}	12	1.02
	K^{+}	12	1.38
	Rb^{+}	12	1.52
B site	Pb^{2+}	6	1.20
	Sn^{2+}	6	1.18
	Ge^{2+}	6	0.73
	Mn^{2+}	6	0.67(low spin), 0.83 (high spin)
	Ca^{2+}	6	1.00
	Ba^{2+}	6	1.35
	Sr^{2+}	6	1.13
	Zn^{2+}	6	0.74
	Sb^{3+}	6	0.76
	Bi^{3+}	6	1.03
	Eu^{3+}	6	0.95
	Eu^{2+}	6	1.09
	In^{3+}	6	0.80
	Yb^{3+}	6	0.86
	Er^{3+}	6	0.88
	Ho^{3+}	6	0.94
	Tb^{3+}	6	0.92
	Sm^{3+}	6	0.96
	Ag^{+}	6	1.15
X site	I^{-}	6	2.20
	Br^{-}	6	1.96
	Cl^{-}	6	1.81

* The sixfold coordination is an essential condition to form the perovskite structure.[12]

Table 2. The physical properties of several representative $CsBX_3$ perovskite materials[12,26,28,30-34,39,157-159]

Physical properties	$CsPbI_3$	$CsPbI_2Br$	$CsPbBr_3$	$CsSnI_3$
Cubic lattice constant (Å)	a=6.201	–	a=5.874	a=6.2057
Optical bandgap Eg (eV)	1.73	1.92	2.30	1.30
Exciton binding energy R* (meV)	15±1[a] / 20[c]	22±3[a]	33±1[d] / 40[c]	18[d]
Carrier diffusion length L_d (μm)	~1[a]	–	0.08[a] / ~10[b]	0.016[a] / ~1[e]
Absorption coefficient (cm^{-1})	$>10^4$	$>10^4$	$9.8*10^4$ [b]	10^5
Carrier mobility μ ($cm^2 V^{-1} s^{-1}$)	25[a]	10[a]	38[a] / >1000[b]	585 (hole)[b] 536(electron)[b]
Dielectric constant ε_{eff} (at 2 K)	10.0[a]	8.6[a]	7.3[d]	–
Charge lifetime (ns)	>20[a] / 10000[d]	14[a]	2000~7000[b]	0.05-19.7[a] / 6.6[e]

* **a**: Spin-coating/solution-processed polycrystalline film. **b**: Single crystals. **c**: Nanocrystal film. **d**: Evaporated polycrystalline film.
* **e**: A melt-synthesized film.

Table 3. The energy-band and the processing solvents of HTM and ETM in $CsBX_3$ PSCs. HOMO: highest occupied molecular orbital, LUMO: lowest unoccupied molecular orbital, VBM: valence band maximum, CBM: conduction band minimum, CB: chlorobenzene. DI-water: deionized water.

Materials		Energy-band		Frequently-used processing solvents
		HOMO or **VBM**	**LUMO** or **CBM**	
HTM	Spiro-OMeTAD	-5.22	-2.4	CB
	PEDOT:PSS	-5.0	–	DI-water or CB or Toluene
	PTAA	-5.14	–	CB
	NiO_x nanoparticle	-5.5	–	DI-water or Alcoholic solution
ETM	TiO_2	-7.3	-4.0	Alcoholic solution
	SnO_2 nanoparticle	-7.92	-4.43	DI-water
	ZnO	-7.41	-4.21	Alcoholic solution
	PCBM	-6.1	-4.3	CB or DI-water or Alcoholic solution

Table 4. Performance parameters of lead-based $CsPbX_3$ perovskite solar cells

Perovskite	Deposition method and atmosphere	Device structure (Optimized strategy)	V_{OC} (V)	J_{SC} (mA/cm^2)	FF (%)	PCE (%)	Ref.
$CsPbI_3$	Solution Air-free	ITO/PEDOT:PSS/Pero/PCBM/Al (A-site Cs-element substitution)	0.79	0.26	45.0	0.09	[49]
$CsPbI_3$	Solution Air-free	FTO/TiO_2/Pero/Spiro-OMeTAD/Au (HI additive)	0.85	12.0	28.4	2.9	[50]
$CsPbI_3$	QD solution Open-air	FTO/TiO_2/Pero/Spiro-OMeTAD/MoOx/Al (Nanocrystals)	1.23	13.47	65.0	10.77	[8]
$CsPbI_3$	Solution Air-free	FTO/TiO_2/Pero/Spiro-MeOTAD/Au (Ascorbic acid additive)	1.08	16.44	64.43	11.44	[51]
$CsPbI_3$	Solution Air-free	FTO/c-TiO_2/mp-TiO_2/Pero/Spiro-MeOTAD/Au (PVP additive)	1.11	14.88	65.0	10.74	[52]
$CsPbI_3$	Solution Air-free	ITO/PTAA/Pero/PCBM/C_{60}/BCP/Cathode (Sulfobetaine zwitterions additive)	1.08	14.9	70.0	11.4	[53]
$CsPb_{0.96}Bi_{0.04}I_3$	Solution Air-free	FTO/c-TiO_2/Pero/CuI/Au (B-site Bi-element doping)	0.97	18.76	72.6	13.21	[54]
$CsPb_{0.95}Ca_{0.05}I_3$	Solution Air-free	FTO/c-TiO_2/mp-TiO_2/Pero/P3HT/Au (B-site Ca-element doping)	0.94	17.3	77.7	12.6	[57]
$CsPbI_3$:5%Eu^{3+}	Solution Open-air	FTO/TiO_2/Pero/Spiro-OMeTAD/Au ($EuCl_3$ doping)	0.90	11.1	68	6.8	[59]
$CsPb_{0.96}Sb_{0.04}I_3$	Solution Open-air	FTO/c-TiO_2/mp-TiO_2/m-Al_2O_3/Pero/Carbon (B-site Sb-element doping)	0.73	14.65	50	5.31	[60]
$Cs_{0.95}Na_{0.05}PbI_3$	Solution Air-free	FTO/TiO_2/Pero/Carbon (A-site Na-element doping)	0.92	16.5	70.3	10.7	[61]
$CsPbI_3$-0.025EDAPbI_4	Solution Air-free	FTO/TiO_2/Pero/Spiro-OMeTAD/Ag (EDA^+ - Crystal dimensionality 'quasi-2D')	1.15	14.53	0.71	11.86	[62]
$PEA_2Cs_{n-1}Pb_nI_{3n+1}$	Solution Air-free	ITO/SnO_2/Pero/Spiro-OMeTAD/Au (PEA^+ - Crystal dimensionality 'quasi-2D')	1.07	16.59	70.0	12.4	[63]
$CsPbI_3$	Solution Dry-air	ITO/SnO_2/Pero/Spiro-OMeTAD/Au (Solvent-controlled crystal growth)	1.08	18.41	79.3	15.71	[64]
$CsPbI_3$	Solution Air-free	FTO/TiO_2/PTABr-Pero/Spiro-OMeTAD/Ag (PTABr Surface post-treatment)	1.10	19.15	80.6	17.06	[65]
$CsPbI_3$	Solution Air-free	FTO/c-TiO_2/PEAI-Pero/Spiro-OMeTAD/Ag (PEAI Surface post-treatment)	1.11	18.50	69.6	14.3	[66]
$CsPbI_3$	Solution Air-free	FTO/TiO_2/Pero/PTAA/Au (HI and PEAI additives)	1.06	18.95	74.9	15.07	[67]
$CsPbI_3$	Solution Dry-air	FTO/c-TiO_2/CHI-Pero/Spiro-OMeTAD/Ag (CHI Surface post-treatment)	1.11	20.23	82.0	18.4	[68]

$CsPbI_3$	Solution Dry-air	FTO/c-TiO_2/Pero/Spiro-OMeTAD/Ag (DMAI volatile additive)	1.14	20.23	82.7	19.03	[9]
$CsPbI_3$	Solution Air-free	FTO/PTAA/Pero/PCBM/BCP/Ag (Organic ligands additive)	1.12	15.81	75.19	13.32	[160]
$CsPbI_3$	Solution Air-free	FTO/c-TiO_2/γ-Pero/P3HT/Au (MA^+/Cs^+ cation exchange)	1.02	17.4	79.4	14.1	[161]
$CsPbI_3$	Solution Air-free	FTO/TiO_2/Pero/Spiro-OMeTAD/Au (Soft template-controlled crystal growth)	1.09	18.29	80.5	16.04	[162]
$CsPbBr_3$	Solution Open-air	FTO/c-TiO_2/mp-TiO_2/Pero/PTAA/Au (Different HTL - interface engineering)	1.28	6.24	74	5.95	[69]
$CsPbBr_3$	Solution Open-air	FTO/d-TiO_2/mp-TiO_2/Pero/PTAA/Au (A-site ion substitution)	1.25	6.7	73	6.2	[70]
$CsPbBr_3$	Solution Open-air	FTO/TiO_2/Pero/Carbon (HTL-free & Carbon electrode)	1.29	5.7	68	5.0	[71]
$CsPbBr_3$	Solution Open-air	FTO/c-TiO_2/m-TiO_2/Pero/Carbon (HTL-free)	1.24	7.4	73	6.7	[72]
$CsPbBr_3$	Solution Open-air	FTO/GQDs/Pero/PQDs/Carbon (HTL- and ETL-free & Interface modification)	1.21	5.08	66.7	4.10	[73]
$CsPbBr_3$	Solution Open-air	FTO/c-TiO_2/m-TiO_2/GQDs/Pero/Carbon (Crystal engineering & Interface modification)	1.46	8.12	82.1	9.72	[74]
$Cs_{0.98}Li_{0.02}PbBr_3$	Solution Open-air	FTO/c-TiO_2/m-TiO_2/Pero/Carbon (A-site Li-element doping)	1.45	6.95	77.9	7.87	[75]
$Cs_{0.94}Na_{0.06}PbBr_3$	Solution Open-air	FTO/c-TiO_2/m-TiO_2/Pero/Carbon (A-site Na-element doping)	1.49	6.97	80.0	8.31	[75]
$Cs_{0.92}K_{0.08}PbBr_3$	Solution Open-air	FTO/c-TiO_2/m-TiO_2/Pero/Carbon (A-site K-element doping)	1.51	7.25	78.4	8.61	[75]
$Cs_{0.91}Rb_{0.09}PbBr_3$	Solution Open-air	FTO/c-TiO_2/m-TiO_2/Pero/Carbon (A-site Rb-element doping)	1.55	7.73	82.2	9.86	[75]
$CsPb_{0.97}Yb_{0.03}Br_3$	Solution Open-air	FTO/c-TiO_2/m-TiO_2/Pero/Carbon (B-site Yb-element doping)	1.54	7.45	80.2	9.20	[76]
$CsPb_{0.97}Er_{0.03}Br_3$	Solution Open-air	FTO/c-TiO_2/m-TiO_2/Pero/Carbon (B-site Er-element doping)	1.56	7.46	82.8	9.66	[76]
$CsPb_{0.97}Ho_{0.03}Br_3$	Solution Open-air	FTO/c-TiO_2/m-TiO_2/Pero/Carbon (B-site Ho-element doping)	1.57	7.45	83.2	9.75	[76]
$CsPb_{0.97}Tb_{0.03}Br_3$	Solution Open-air	FTO/c-TiO_2/m-TiO_2/Pero/Carbon (B-site Tb-element doping)	1.59	7.47	84.8	10.06	[76]
$CsPb_{0.97}Sm_{0.03}Br_3$	Solution Open-air	FTO/c-TiO_2/m-TiO_2/Pero/Carbon (B-site Sm-element doping)	1.59	7.48	85.1	10.14	[76]
$CsPbBr_3$	QD solution Open-air	FTO/TiO_2/Pero/Spiro-OMeTAD/Au (Nanocrystals)	1.50	5.6	62.0	5.4	[77]

$CsPbBr_3$	Solution Open-air	FTO/TiO_2/CQD-Pero IO/Spiro-OMeTAD/Ag (Processing engineering)	1.06	11.34	69.0	8.29	[78]
$CsPbBr_3$	Solution Open-air	FTO/TiO_2/Pero/$CuInS_2$-ZnS QDs/Carbon (Interface modification)	1.45	7.47	77.7	8.42	[79]
$CsPbBr_3$	Solution Open-air	FTO/TiO_2/GQDs/Pero/$CuInS_2$-ZnS QDs/Carbon (Interface modification)	1.52	7.35	84.3	9.43	[80]
$CsPbBr_3$	Solution Open-air	FTO/SnO_2 QDs/Pero/$CsSnBr_3$ QDs/Carbon (Interface modification)	1.61	7.80	84.4	10.60	[81]
$CsPbBr_3$	Solution Open-air	FTO/SnO_2 QDs/Pero/$CsBi_{2/3}Br_3$ QDs/Carbon (Interface modification)	1.594	7.75	80.9	10.0	[81]
$CsPbBr_3$	Solution Open-air	FTO/SnO_2 QDs/Pero/$CsCuBr_3$ QDs/Carbon (Interface modification)	1.556	7.68	78.2	9.34	[81]
$CsPbBr_3$	Solution Open-air	FTO/c-TiO_2/m-TiO_2/Pero/$CsSnBr_{3-x}I_x$ QDs/Carbon (Interface modification)	1.39	8.70	75.5	9.13	[82]
$CsPb_{0.97}Sm_{0.03}Br_3$	Solution Open-air	FTO/TiO_2/Pero/Cu(Cr,Ba)O_2 NCs/Carbon (Interface modification)	1.62	7.81	85.5	10.79	[83]
$CsPbBr_3$	Solution Open-air	FTO/c-TiO_2/m-TiO_2/Pero/Cu_2ZnSnS_4/Ag (HTL interface engineering)	0.94	7.36	70.0	4.84	[163]
$CsPbBr_3$	Solution Open-air	FTO/TiO_2/Pero/C12-$CuInS_2$@ZnS QDs/LPP-Carbon (HTL interface engineering & Fluorescent Carbon)	1.626	7.73	86.3	10.85	[164]
$CsPbBr_3$-$CsPb_2Br_5$	Evaporation Air-free	FTO/TiO_2/Pero/Spiro-OMeTAD/Ag (Self-passivation)	1.30	8.48	75.9	8.34	[85]
$CsPbBr_3$	Solution Open-air	ITO/TiO_2/Pero/Spiro-OMeTAD/Au (NH_4SCN additive)	1.375	7.76	79.3	8.47	[86]
$CsPbBr_3$	Evaporation Air-free	ITO/ZnO/Pero/Spiro-MeOTAD/Au (Top cell of Tandem solar cell)	1.44	7.01	77.1	7.78	[87]
$CsPb_{0.97}Tb_{0.03}Br_3$	Solution Open-air	FTO/c-TiO_2/m-TiO_2/Pero/SnS:ZnS/NiOx/Carbon (Integrated solar cell)	1.57	8.21	79.6	10.26	[158]
$CsPbBr_3$	Solution Air-free	FTO/c-TiO_2/m-TiO_2/Pero/Spiro-OMeTAD/Au (Pyridine-vapor treatment)	1.34	6.52	69	6.05	[165]
$CsPbI_2Br$	Solution Air-free	FTO/TiO_2/Pero/Spiro-MeOTAD/Ag (Composition engineering)	1.11	11.89	75.0	9.84	[88]
$CsPbI_2Br$	Solution Air-free	ITO/PEDOT:PSS/Pero/PCBM/BCP/Al (Composition engineering)	1.06	10.9	–	6.80	[89]
$Cs_{0.925}K_{0.075}PbI_2Br$	Solution Air-free	FTO/bl-TiO_2/Pero/Spiro-MeOTAD/Au (A-site K-element doping)	1.18	11.6	73.0	10.0	[90]
$CsPb_{0.98}Sr_{0.02}I_2Br$	Solution Air-free	FTO/c-TiO_2/mp-TiO_2/Pero/P3HT/Au (B-site Sr-element doping)	1.04	15.3	69.9	11.2	[91]
$CsPb_{0.75}Sn_{0.25}IBr_2$	Solution Air-free	ITO/SnO_2/C_{60}/Pero/Spiro-OMeTAD/Au (B-site Sn-element doping)	1.21	12.57	75.8	11.53	[92]

$CsPb_{0.9}Sn_{0.1}IBr_2$	Solution Air-free	FTO/c-TiO_2/m-TiO_2/Pero/Carbon (B-site Sn-element doping)	1.26	14.3	63	11.33	[93]
$CsPb_{0.995}Mn_{0.005}I_{1.01}Br_{1.99}$	Solution Air-free	FTO/c-TiO_2/m-TiO_2/Pero/Carbon (B-site Mn-element doping)	0.99	13.15	57	7.36	[94]
$CsPbI_2Br$-2% $MnCl_2$	Solution Air-free	FTO/TiO_2/Pero/$CsPbI_2Br$ QDs/PTAA/Au (B-site Mn-element doping)	1.17	14.37	80.0	13.47	[95]
$CsPb_{0.95}Eu_{0.05}I_2Br$	Solution Dry-air	FTO/c-TiO_2/mp-TiO_2/Pero/Spiro-OMeTAD/Au (B-site Eu-element doping)	1.22	14.63	76.6	13.71	[96]
$CsPbI_2Br$-0.25% $InCl_2$	Solution Air-free	FTO/NiOx/Pero/ZnO@C60/Ag (B-site In-element doping)	1.14	15.7	77	13.74	[97]
$CsPbI_3$:Br:InI_3	Solution Open-air	FTO/c-TiO_2/m-TiO_2/Pero/Carbon (B-site In-element doping)	1.20	15.68	64	12.04	[98]
$CsPbI_2Br$-0.2wt% $CuBr_2$	Solution Air-free	FTO/TiO_2/Pero/Spiro-OMeTAD/MoO_3/Ag (B-site Cu-element doping)	1.18	16.95	80	16.15	[99]
$CsPb_{0.8}Ge_{0.2}I_2Br$	Solution Open-air	FTO/SnO_2/Pero/P3HT/Spiro-OMeTAD/Au (B-site Ge-element doping)	1.27	12.15	70.1	10.8	[100]
CsPb(Ba)IBr_2	Solution Air-free	FTO/TiO_2/Pero/Spiro-OMeTAD/Au (B-site Ba-element doping)	1.19	11.91	0.74	10.51	[101]
$CsPbI_2Br$-7.5% Zn^{2+}	Solution Air-free	ITO/SnO_2/Pero/Spiro-OMeTAD/MoO_3/Ag (B-site Zn-element doping)	1.24	15.61	63.0	12.16	[102]
$CsPb_{0.9}Zn_{0.1}I_2Br$	Solution Air-free	FTO/c-TiO_2/Pero/Spiro-OMeTAD/Ag (B-site Zn-element doping)	1.18	15.8	72.7	13.6	[103]
$CsPb_{1-x}Ba_xI_2Br$	Solution Dry-air	FTO/c-TiO_2/m-TiO_2/Pero/Spiro-OMeTAD)/Au (B-site Ba-element doping)	1.28	14.0	78.2	14.0	[104]
$CsPbI_2Br$	Solution Air-free	ITO/SnO_2/ZnO/Pero/Spiro-OMeTAD/MoO_3/Ag (ETL interface engineering)	1.23	15.0	78.8	14.6	[105]
$CsPbI_2Br$	Solution Air-free	ITO/SnO_2@ZnO/Pero/Spiro-OMeTAD/MoO_3/Ag (ETL interface engineering)	1.11	16.45	79	14.35	[106]
$CsPbI_2Br$	QD solution Open-air	ITO/TiO_2/Pero/P3HT/Au (HTL interface engineering)	1.30	13.13	70.4	12.02	[107]
$CsPbI_2Br$	Solution Air-free	FTO/NiOx/Pero/ZnO@C60/Ag (ETL interface engineering)	1.14	15.2	77	13.3	[108]
$CsPbI_2Br$	Solution Air-free	ITO/ZnO/SnO_2/Pero/H-Z2/MoO_3/Ag (HTL interface engineering)	1.28	14.7	76.4	14.4	[166]
$CsPbI_2Br$	Solution Air-free	ITO/SnO_2/Pero/Co_3O_4/Carbon (HTL interface engineering)	1.187	13.09	72.12	11.21	[167]
$CsPbI_xBr_{3-x}$	Solution Air-free	ITO/SnO_2/LiF/Pero/Spiro-OMeTAD/Au (Interface engineering)	1.23	18.3	82.6	18.64	[109]
$CsPbI_2Br$	Solution Air-free	FTO/c-TiO_2/m-TiO_2/Pero/Bi_2Te_3/Spiro-OMeTAD/Ag (Interface engineering)	1.14	14.80	71	11.96	[110]

$CsPbIBr_2$	Solution Air-free	ITO/SnO_2/$SnCl_2$/Pero/YD_2-o-C8/Spiro-OMeTAD/Au (Interface engineering)	1.37	12.05	61	10.13	[111]
$CsPbI_2Br$	Solution Air-free	FTO/TiO_2/PEACl-Pero/PTAA/Au (PEACl Surface post-treatment)	1.227	14.55	78.7	14.05	[168]
$CsPbI_xBr_{3-x}$	Solution Air-free	ITO/NiOx/(6TIC-4F)-Pero/ZnO/C_{60}/Ag (6TIC-4F Surface post-treatment)	1.16	17.70	78.6	16.10	[112]
$CsPbI_2Br$	Solution Air-free	ITO/SnO_2/Pero/CsBr/Spiro-OMeTAD/Au (Interface modification & $Pb(Ac)_2$ additive)	1.27	16.72	77.2	16.37	[113]
$CsPbIBr_2$	Solution Air-free	FTO/TiO_2/Pero/GAI/Spiro-OMeTAD/Au (Interface modification)	1.20	10.24	74.6	9.17	[114]
$CsPbI_2Br$	Solution Air-free	FTO/TiO_2/Pero/$CsPbI_2Br$ QDs/FAI/PTAA/Au (Interface modification)	1.22	14.51	79.6	14.12	[116]
$CsPbI_2Br$	Solution Air-free	ITO/SnO_2/PN4N/Pero/PDCBT/MoO_3/Ag (ETL interface engineering)	1.30	15.3	81.5	16.2	[118]
$CsPb(I_{0.85}Br_{0.15})_3$	Solution Air-free	ITO/SnO_2/Pero/Spiro-OMeTAD/Au (Solvent-controlled crystal growth)	1.22	17.3	77.5	16.14	[64]
$CsPbI_2Br$	Solution Air-free	ITO/c-TiO_2/Pero/Spiro-MeOTAD/Au (ATS/GTA-controlled crystal growth)	1.23	16.79	77.8	16.1	[119]
$CsPbI_2Br$	Solution Air-free	ITO/SnO_2/Pero-80 mmol% CsI/Carbon (Cocrystallization - spinodal decomposition method)	1.19	12.91	66.1	10.13	[117]
$CsPbI_2Br$	Solution Air-free	FTO/c-TiO_2/Pero/Spiro-OMeTAD/Ag ($HPbI_{3+x}$ - low temperature perovskite fabrication)	1.13	16.61	68.64	10.56	[169]
$CsPbIBr_2$	Solution Open-air	FTO/c-TiO_2/mp-TiO_2/Pero/Spiro-MeOTAD/Au (Spray-assisted deposited method)	1.12	7.9	70.0	6.3	[125]
$CsPbI_2Br$	Solution Open-air	FTO/c-TiO_2/Pero/Spiro-MeOTAD/Au (Blade-coating method)	1.15 1.17	16.41 15.25	75.1 67.4	14.69 12.52	[126]

Table 5. Summary of performance parameters reported for lead-free $CsBX_3$ perovskite solar cells

Perovskite	Deposition method and atmosphere	Device structure (Optimized strategy)	V_{OC} (V)	J_{SC} (mA/cm^2)	FF (%)	PCE (%)	Ref.
$CsSnI_3$	Evaporation Air-free	ITO/Pero/Au/Ti (A Schottky solar cell)	0.42	4.80	22	0.88	[6]
$CsSnI_3$	Solution Air-free	FTO/c-TiO_2/m-TiO_2/Pero/m-MTDATA/Au (20mol% SnF_2 additive)	0.24	22.70	37	2.02	[7]
$CsSnI_3$	Solution Air-free	ITO/NiO_x/Pero/PCBM/Al (Interface and solvent engineering)	0.52	10.21	62.5	3.31	[128]
$CsSnI_3$	Solution Air-free	ITO/Pero-SnX_2/$PC_{61}BM$/BCP/Al (10mol% $SnCl_2$ additive)	0.51	10.44	69	3.56	[129]
$CsSnI_3$	Solution Air-free	FTO/d-TiO_2/Pero-SnX_2/PTAA/Au (10mol% $SnBr_2$ additive)	0.44	18.5	52.9	4.30	[130]
$CsSnI_3$	Solution Air-free	FTO/c-TiO_2/m-TiO_2/Pero/PTAA/Au (Excess SnI_2 & N_2H_4 atmosphere)	0.38	25.71	49.1	4.81	[131]
$CsSn_{0.5}Ge_{0.5}I_3$	Evaporation Air-free	FTO/PCBM/Pero/native oxide/Spiro-OMeTAD/Au (Interface passivation)	0.63	18.61	60.6	7.11	[132]
$CsSnBr_3$	Solution Air-free	FTO/d-TiO_2/m-TiO_2/Pero/Spiro-OMeTAD/Au (20mol% SnF_2 additive)	0.42	9.10	57	2.17	[134]
$CsSnBr_3$	Solution Air-free	FTO/c-TiO_2/m-TiO_2/Pero/PTAA/Au (N_2H_4 atmosphere & 20mol% SnF_2 additive)	0.37	13.96	59.4	3.04	[135]
$CsSnBr_3$	Solution Air-free	FTO/TiO_2/Pero/Spiro-OMeTAD/Au (Composition engineering & SnF_2 additive)	0.41	3.99	58	0.95	[136]
$CsSnBr_3$	Evaporation Air-free	ITO/MoO_3/Pero/C_{60}/BCP/Ag (2.5mol% SnF_2 additive)	0.5	2.3	57	0.55	[137]
$CsSnI_{2.9}Br_{0.1}$	Solution Air-free	FTO/TiO_2/Pero/Spiro-OMeTAD/Au (Composition engineering & SnF_2 additive)	0.22	24.16	33	1.76	[136]
$CsSnIBr_2$	Solution Air-free	FTO/TiO_2/Al_2O_3/Pero/Carbon (HPA additive)	0.35	17.4	55.0	3.20	[138]
$CsGeI_3$	Solution Air-free	ITO/TiO_2/Pero/Spiro-OMeTAD/Au	0.07	5.7	27	0.11	[140]
$Cs_2SnI_4Br_2$	Solution Open-air	FTO/TiO_2/Sn-TiO_2/Pero/Cs_2SnI_6 HTM/LPAH/FTO (Composition engineering)	0.563	6.225	57.7	2.025	[141]
Cs_2TiBr_6	Evaporation Air-free	FTO/TiO_2/C_{60}/Pero/P3HT/Au (Low-temperature vapor-based method)	1.02	5.69	56.4	3.28	[142]
Cs_2NaBiI_6	Solution Air-free	FTO/c-TiO_2/m-TiO_2/Pero/Spiro-OMeTAD/Au	0.47	1.99	44	0.42	[143]
$Cs_2AgBiBr_6$	Solution Air-free	FTO/TiO_2/Pero/Spiro-OMeTAD/MoO_3/Ag (Composition stoichiometry)	1.01	3.82	65	2.51	[144]

$Cs_2AgBiBr_6$	Evaporation Air-free	FTO/TiO_2/Pero/Spiro-OMeTAD/MoO_3/Ag	1.05	2.06	65	1.41	[144]
$Cs_3Bi_2I_9$	Solution Air-free	FTO/c-TiO_2/Pero/CuI/Ag	0.86	5.78	64.38	3.20	[145]
$Cs_3Sb_2I_9$	Solution Air-free	ITO/PEDOT:PSS/Pero/$PC_{70}BM$/Al	0.72	5.31	38.97	1.49	[146]
$Cs_2AgBiBr_6$	Solution Open-air	FTO/c-TiO_2/m-TiO_2/Pero/Spiro-OMeTAD/Au (Perovskite annealing conditions optimization)	0.98	3.93	63	2.43	[147]
$Cs_2AgBiBr_6$	Evaporation Air-free	FTO/c-TiO_2/Pero/P3HT/Au	1.12	1.79	68	1.37	[148]
Cs_2SnI_6	Solution Open-air	FTO/TiO_2/Pero/P3HT/Ag	0.256	7.41	24.5	0.47	[150]



Jingjing Tian received her B.S. degree (2017) in School of Materials Science and Engineering from Wuhan University of Technology (WHUT). Now she is a master student in School of Materials Science and Engineering from South China University of Technology (SCUT) under the supervision of Prof. Hin-Lap Yip. Her research mainly focuses on materials, interface and device engineering for high efficiency and stable all-inorganic perovskite solar cells.



Qifan Xue received his B.S. degree (2013) and Ph.D. degree (2017) in School of Materials Science and Engineering from South China University of Technology (SCUT) under the supervision of Prof. Hin-Lap Yip and Prof. Yong Cao. He became a lecturer at the State Key Laboratory of Luminescent Materials and Devices of SCUT in 2017 and was promoted to Associate Professor in 2019. His research focuses on interface, materials and device engineering for highly efficient polymer solar cells and perovskite solar cells.



Hin-Lap Yip is a Professor in the State Key Laboratory of Luminescent Materials and Devices and

the Materials Science and Engineering (MSE) Department in South China University of Technology (SCUT). He studied MSE at the Chinese University of Hong Kong (BSc 2001 and MSc 2003) and completed his PhD degree in MSE in 2008 under the guidance of Prof. Alex Jen at the University of Washington, Seattle. He then worked as a postdoctoral researcher at the same group before joining SCUT in 2013. His main research interests are in the fields of polymer and perovskite optoelectronic materials and devices.

Recent progress in inorganic lead-based and lead-free $CsBX_3$ PSCs is reviewed combined with various strategies and their prospects and challenges presented in the future are discusses in detail.

Keywords: lead-based and lead-free, inorganic perovskite solar cells, fundamental properties, progress, challenges

Jingjing Tian[1], Qifan Xue[1,2], Qin Yao[1], Ning Li[3,4,5], Christoph J. Brabec[3,4], Hin-Lap Yip[1,2]**

Inorganic Halide Perovskite Solar Cells: Progress and Challenges

